



POLITECNICO
MILANO 1863

SCUOLA DI INGEGNERIA INDUSTRIALE
E DELL'INFORMAZIONE

Numerical study of the impact of nozzle shape on underexpanded jet - wall interaction

TESI DI LAUREA MAGISTRALE IN
AERONAUTICAL ENGINEERING - INGEGNERIA AERONAUTICA

Author: **Roberto D'Angelo**

Student ID: 941414

Advisor: Prof. Luigi Vigevano

Co-advisors: Prof. Koen Hillewaert (ULiège)

Academic Year: 2021-22

Abstract

A numerical investigation concerning axisymmetric underexpanded turbulent flow issuing from a convergent-divergent nozzle is carried out by means of Reynolds averaged Navier-Stokes (RANS) equations and is contained in this work. The numerical computations are performed making use of the in-built axisymmetric solver of the open-source CFD software SU2 and regard the outflow expansion in case of jet release in a quiescent environment and in case of jet impingement on a flat plate. By doing so, this work proposes to investigate if the free-flow and impinging flow structures are sensitive to the shape of the nozzle used to accelerate the fluid, and if yes, to which extent. This is accomplished by considering three different nozzles: one contoured and two conical nozzles with different lengths. To cover a wider range of configuration, the nozzle-pressure-ratio (NPR) and the nozzle-to-plate distance are also varied. From the investigation of the flow field, it is found that the intensity of the shocks contained in both the core region and the impinging region of the jet are affected by the nozzle geometry, while the evolution of the radial wall-jet generated by the jet impingement is instead found to have rather small sensitivity. Validation and verification of the code is also performed in advance by replicating real experimental tests and comparing the obtained results with other numerical simulations found in literature.

Keywords: Underexpanded jets, Impinging jets, CFD, SU2

Abstract in lingua italiana

Un'indagine numerica relativa a flussi turbolenti assial-simmetrici sottoespansi rilasciati da un ugello convergente-divergente è stata effettuata mediante equazioni di Navier-Stokes mediate (RANS) ed è contenuta in questo lavoro. I calcoli numerici sono stati eseguiti utilizzando il risolutore assial-simmetrico integrato nel software CFD open-source SU2 e riguardano l'espansione esterna del flusso in caso di rilascio in ambiente quiescente e in caso di impatto a velocità supersonica su una superficie piana. In questo modo, questo lavoro si propone di indagare se le strutture del getto sottoespanso e del getto impattante su una superficie piana sono sensibili alla forma dell'ugello utilizzato per accelerare il fluido e, in caso affermativo, in quale misura. Ciò è stato realizzato considerando tre diversi ugelli: uno sagomato e due ugelli conici di diverse lunghezze. Per coprire una più ampia gamma di configurazioni, sono stati variati anche il rapporto pressione ugello e la distanza ugello-superficie. Dall'indagine del campo di flusso, è stato ottenuto che l'intensità degli urti contenuti sia nella regione centrale che in quella di impatto del getto sono influenzati dalla geometria dell'ugello, mentre l'evoluzione del getto radiale sulla superficie piana conseguenza dall'impatto del flusso risulta invece essere meno influenzato dalla geometria. La validazione e la verifica del codice sono state preventivamente realizzate provando l'indipendenza dei risultati dalla griglia di calcolo e replicando prove sperimentali reali e confrontando i risultati ottenuti con altre simulazioni numeriche presenti in letteratura.

Parole chiave: Flussi sottoespansi, impatto supersonico su una parte piana, CFD, SU2

Contents

Abstract	i
Abstract in lingua italiana	iii
Contents	v
1 Introduction	1
2 Theory	5
2.1 Research and applications	5
2.2 Physics	7
2.3 Underexpanded free jet structure	8
2.3.1 Nearfield zone	10
2.3.2 Transition and farfield zone	14
2.4 Impinging flow structure	14
3 Method	19
3.1 Numerical method	19
3.1.1 Governing equations for compressible flow	19
3.1.2 RANS approach	20
3.2 Numerics	24
3.3 Mesh set-up	25
4 Verification and validation	29
4.1 Free flow validation	29
4.1.1 Case description	29
4.1.2 Grid independence analysis	31
4.1.3 Results	33
4.1.4 Numerical Uncertainties	37
4.2 Impinging flow validation	38

4.2.1	Case description	38
4.2.2	Grid independence analysis	40
4.2.3	Results	41
4.2.4	Numerical uncertainties	45
4.3	Conclusions	46
5	Tests and Results	49
5.1	Test Cases	49
5.2	Results	53
5.2.1	Free flow configuration	53
5.2.2	Impinging flow	60
6	Conclusion and improvements	71
	Bibliography	73
	List of Figures	79
	List of Tables	83
	Acknowledgements	85

1 | Introduction

The interaction of a high-speed jets with the ground is nowadays of great interest because of the numerous engineering application where it is involved and plays a key role. Indeed, such interaction, commonly referred as *ground effect*, has strong implications on many fluid-dynamic and thermodynamic critical aspects of the technologies where it is involved, not only in aerospace applications but also in several other industrial fields.

Among others, jet impingement can be observed in contexts such as control of heat transfer (enhancing or suppressing the heat) in gas turbines materials or cooling of electric components [1–3], various manufacturing processes like thermal sprays [4], as well as in many aerospace applications like STOVL (Short Take-Off and Vertical Landing) aircraft hovering near the ground [5, 6] and, last but not least, launching and landing of aircraft and spacecrafts [7–9].

Indeed, the ground effects has a remarkable importance when a rocket launches or lands, due to the high loads exerted on impinged structures. Indeed, during rocket ascending or descending operations, the engine exhaust gases impact on the launch structure, consisting of different parts like the launch platform and the jet deflectors, leading to the generation of a complex flow field. The jet impacting on the platforms lying beneath the rocket is consequently responsible for large aerodynamic and thermodynamic loads, that have to be carefully predicted during design phase. Indeed, the possible overload consequence of the impinging jet can undermine safe launch/landing operations. Hence, become of fundamental importance the correct prediction of the flow field.

The main features concerning the risk prediction and control are linked to the overall structures of the jet, especially pressure, temperature and velocity levels attained in the surrounding. It is well know that it exists a strong connection between all of this factors and the developed shock waves pattern, which hence necessitate an in-depth analysis.

Furthermore, the interaction of the flow issuing from a nozzle with the ground (or an off-shore platform) is nowadays of great interest for stability reasons not only concerning take-off but also for landing manoeuvres and even re-usability purposes, which is now proposed as a viable technical solution.

For all the above-mentioned reasons, the physics of free and impinging supersonic jets

has been widely investigated by many researches throughout the years, both numerically and experimentally. Much effort has been made in the direction of understanding the characterising features of such phenomena, in order to have a complete picture of the physics and of the critical aspects.

However, this kind of flow are rather complex and far from being completely understood. Indeed they include many interesting phenomena concerning fluid-dynamics such as co-existence of subsonic and supersonic regions, shock/shock interactions, shock/boundary layer interactions and embedded shear layer, among others. Moreover, multiple shocks structures consisting of barrel, plate and reflected shocks are generated, as well as the instability of what is known as *stagnation bubble*, a recirculation region which may be observed in the impingement region in some conditions.

Additionally, the flow field generated by the exhaust gases impingement on a surface behaves differently with respect to the height, which is commonly defined as the distance between the nozzle exit section and the beneath platform. As a consequence, flow field properties and loads change dynamically during the rocket operations.

It is also known empirically that localized pressure peaks are observed under certain conditions on the impingement surface over which might cause cracks.

In this regard, it becomes of paramount importance for the design phase to fully access the information on the flow field of engine exhaust impingement and predict the loads accurately. Direct field measurements can provide the needed information on the interaction of the impinging flow with the actual structures in the surroundings in real conditions. However, it can be difficult and expensive to perform such measurements in detail, especially whether different configuration have to be investigated and numerous flow parameters have to be estimated. Also, model experiments with reduced scale can represent a solution. Nevertheless, to preserve the similarity in this cases may constitute a difficulty.

In this context, Computational Fluid Dynamics (CFD) is settling as an established reality in modern engineering applications involving fluids. Indeed, it has been used widely and successfully in several areas of research. In the specific, concerning supersonic jets, Reynolds-Average Navier-Stokes (RANS) solvers are already been proven to be a reliable tool to accomplish numerical simulations.

CFD is also generally more economical compared to experimental methods when one's aim is to investigate a wide range of configurations and obtain measurements of numerous quantities regarding the entire flow field.

However, although a significant number of researches evolved in the direction of better understanding the supersonic impinging jet, there is still a lack of studies using a CFD solvers and experimental setup to investigate the effect of different nozzle geometries on

the shock structures. Also, some critical aspects concerning the flow field are yet to be fully understood, such as the formation of the above-mentioned supersonic bubbles.

In this framework, this work inscribes itself in a joint effort between the laboratory André Jaumotte of the Université Libre de Bruxelles and the University of Liège, aiming to develop an experimental setup to study the ground effect at small scale.

In the specific, one of the main focuses of this study is to further investigate the shock structures within the flow, with particular attention to the nozzle pressure ratio (NPR) and the nozzle-to-wall distance and especially if, and if so, to which extent the nozzle geometry has an impact on the development of the flow field of the supersonic impinging jet. With this regard, three different converging-diverging axisymmetric nozzle have been numerically investigated in ground effect. The first nozzle, indicated as N1, is a contoured nozzle obtained exploiting the theory of characteristics. The remaining nozzles (N2 and N3) have instead a conical divergent section with different diffusive angle and length.

With this purpose, this work proposes to clarify some peculiar aspects of the flow field, and, specifically, the coupling between the phenomena and the kind of devices used to accelerate the flow.

In particular, the mean properties of the flow field related with the inner jet region and, thus, what is generally considered as a strongly steady region, will be at the center of the effort. Also, beside the jet in real applications may be either axisymmetric or present asymmetries, the present work will concentrate on the former configuration, focusing in particular on round axisymmetric underexpanded turbulent jets.

Additionally, in order to assess the most suitable set-up needed in this kind of computations, the performances of two popular turbulence models will be evaluated in this work. The study hereafter reported has been performed exploiting the CFD open-source code SU2 (C++ based software capable of solving PDE). This tool has already been validated and shows successfully performances in a wide range of fluid-dynamic instances. To perform numerical simulation of high-quality grids, the NIC5 High Performance Computing (HPC) cluster of the University of Liège has been employed.

Thesis outline:

This work is organised as following:

- in Chapter 2 is presented an overview on the physics involved, including the descriptions of both supersonic flows expanding in a open environment and impinging jet issuing from a convergent-divergent nozzle on a flat plate. Additionally, some

interesting applications and researched made in the same context will be briefly described;

- Chapter 3 will then report the numerical method chosen and strategy followed to accomplish the analysis contained in the ensuing sections;
- Chapter 4 is dedicated to the validation and verification of the code and also contains the assessment of the performances of the employed turbulence models;
- in Chapter 5 in contained the final investigation regarding the influence that the nozzle shape may have on the evolution of the flow field in ground effect, depending on different nozzle pressure ratios and nozzle-to-wall distances.

2 | Theory

Aim of this chapter is to review several features of the physics involved during out-flow supersonic expansion in cases of free and impinging supersonic flow, in order to provide an exhaustive basis to understand the analysis performed in the following.

Firstly, an overview of previous works and applications is reported. Then, the phenomena involved in these kinds of flows are discussed in their most important features. In particular, the steady state structures of a free underexpanded jet will be discussed in its general characteristics and behaviour depending on the nozzle pressure ratio. Finally, a discussion on the structures that are expected to form during a supersonic impingement is contained in the last section.

2.1. Research and applications

The flow field of impinging jet is of practical importance on several engineering technologies and has been widely investigated throughout the years. The wide range of application where it is involved, directly or not, makes its full comprehension of crucial importance for aspects such as reliability, safety and optimization of performances.

However, although several studies focused on flow impingement, this research area is still active today and comprehends many critical aspects which are far to be completely understood. This is due to the complexity of such flows which, among others, include *stand-off* or *plate* shocks (in front of the impinged surface), co-existence of supersonic and subsonic region, presence of embedded shear layers, radial wall-jets, potential formation of recirculation area and furthermore shock-shock, shock-boundary layer or shock-shear layer interactions. Additionally, under for high nozzle pressure ratios a normal shock, commonly referred as *Mach disk*, can form in the free underexpanded jet, which has an impact on the flow-ground relationship and further increases its complexity.

Among the extensive amount of available literature, Donaldson and Snedeker [10] in a classic study lay the foundations for the underexpanded jet impingement study, investigating the behavior for a range of nozzle pressure ratio (NPR) and the nozzle-plate distance. They measured the stagnation region pressure distributions, revealing the po-

tential presence of separated flow regions, often called *stagnation bubbles*, under specific conditions of impingement distance and Mach number. Gummer and Hunt [11] experimentally investigated the near-wall flow generated by axisymmetric jets impacting of a flat surface, while Carling and Hunt [12] further explored the results focusing on the near wall jet, being this one the most critical region for practical reasons. A relevant research has been accomplished by Iwamoto [13], which assessed the interaction between nozzle-plate spacing, height of the plate shock and shock-cells length.

Similarly, the ground effect concerning inclined flat plate has found wide interest in the past. Lamont and Hunt [14] performed a well-know experiment analysing the impact of the angle of the plate on the pressure distribution. Goto et. al. [15] replicated numerically the same study, further investigating the formation of pressure peaks on the surface. The classification of the flow with respect to the impingement angle has instead been made by Nakai et. al [16].

Further renowned studies on jet impingement have been performed by Krothapalli et. al. [17], which conducted experiments concerning the loads generated on a plate by an axisymmetric supersonic jet, while Alvi et. al. [18] performed similar studies both numerically and experimentally.

In a more recent research, the formation of stagnation bubble with respect to the nozzle pressure ratio has been numerically predicted and discussed by Kim and Park [19]. A number of numerical studies on this topic have also been published, for instance the computations performed by Chin et. al. [20], which investigated the flow impingement varying the distance and angle of impact, along with the assessment of some popular turbulence models performances.

An additional area of interest concerns acoustic issues related to jet impingement. A consistent number of studies dealt with noise generations, among others B. Henderson et. al. [21] examined the correlation between flow unsteadiness and acoustic tones generation for different configurations.

Interest in ground effects machines as STOVL has also attracted wide research to this field. Indeed, high structural and acoustic loads generate together with down-wash erosion, which can represent an issue needed to be accounted during design phase. Moreover, the out-wash radial flow is of practical concern in cases where hovering happens above confined spaces, as on off-shore platforms. In this area, researchers as Harmon et. al. [6] and Myers et. al. [5] performed experimental investigation aiming to gain a better understanding of the complex dual jet impingement.

The study of ground erosion has then been extended to problems relative to launching rockets or landing devices on lunar or planetary surfaces. In a recent study, Kagenov et. al. [9] investigated the effect of the ExoMars propulsion system configuration of the Mars

surface in order to predict potential surface erosion.

Even the effect of nozzle geometry on the structure of supersonic free jet has been examined throughout the years. As instance, Hatanaka et. al. [22] and Otobe et. al. [23] investigated their correlation, both numerically and experimentally. Additionally, by means of the schlieren method they studied the relation between the Mach disk diameter and the nozzle pressure ratio, concluding that the nozzle geometry can have an impact on the Mach disk height, while the same is not true for its axial position. Despite the wide number of publications dealing with impinging jets, the effect of the nozzle shape on this kind of flows is apparently yet to be investigated.

2.2. Physics

An underexpanded jet is observed whenever a supersonic flow issuing from a device has an outlet pressure greater than the surrounding medium. In this condition, the pressure balance occurs in the open space, where the flow must undergo an expansion at the immediate downstream of the device exit section to match the back pressure. This happens in order to satisfy the boundary condition at the jet edge, being this one the fluid-fluid interface across which the pressure on both the sides must be equal. The distinctive structures generated by this out-flow expansion are dominated by compressible and viscous effects, which compete together in order to define the overall flow pattern.

It is common knowledge that this kind of flow is likely to happen with convergent and convergent-divergent nozzles, as extensively discussed in literature [24, 25]. In particular, in a convergent-divergent device this can happen only when the feeding pressure is such that the throat is sonic so that the flow can evolve in the divergent section as supersonic. In this circumstances, the mass flow depends only on the total conditions, under the assumption of ignoring the small effects due to viscous phenomena inside the device.

The external evolution of the flow field issuing from a nozzle depends, instead, also on the external conditions. In order to quantitatively assess the behaviour of an underexpanded jet based on the pressure ratio, the following quantities are defined:

$$\eta_0 = \frac{P_0}{P_\infty}, \quad (2.1)$$

where P_0 is the total pressure feeding the nozzle, P_∞ is the ambient pressure, and

$$\eta_e = \frac{P_e}{P_\infty}, \quad (2.2)$$

being in this case P_e the pressure at the nozzle outlet section.

From the above discussion, the condition needed in order to observe an underexpanded jet is $\eta_e > 1$. The structure of such flows will be detailed in the following section.

Nevertheless, the exit Mach number and the divergence angle of the jet at the outlet section also may have some influence on the final structure of the jet.

On the other hand, while the behavior of a free jets can be described on the basis of pressure, the full parameter range affecting the impingement of supersonic jets is shown to be wide. The major parameters influencing the phenomena include the initial pattern of the jet (depending on η_e even in this case), the stage of the expansion at the outlet section, the jet Reynolds number (Re_j) and the impingement angle. Anyway, while the former parameters will be discussed in the following, the impact of the impingement angle on the flow is actually out of the purposes of this work and hence will not be detailed.

Moreover, the flow field generated by the exhaust-wall interaction behaves differently depending on the nozzle-to-wall distance, generally normalised with respect to the nozzle outer diameter (z/D , where D is the nozzle exit diameter and z is the distance from the wall). Indeed, the interaction with the ground changes dynamically and can be more or less relevant during ascension/descending phase. In particular, the length of the core region plays an important role in this case: when the distance is large enough, the interaction is weak and the jet can be assumed as a free jet, while at smaller distances the impingement of the flow has critical consequences on the fluid-dynamic and thermodynamic of the phenomena involved.

2.3. Underexpanded free jet structure

The overall structure of a supersonic jet expanding in a free environment has been extensively investigated and is today very well-know. In this section, a review on its steady state is reported, together with a brief description concerning other secondary aspects.

Commonly, the flow field of an underexpanded jet is divided into three regions [26]:

- nearfield zone;
- transition zone;
- farfield zone.

A schematic representation of the flow field zones can be observed in Figure 2.1.

The nearfield zone is, in turn, composed of a potential core and a mixing layer. The core region (also know as gas-dynamic region) is dominated by compressible effects and is

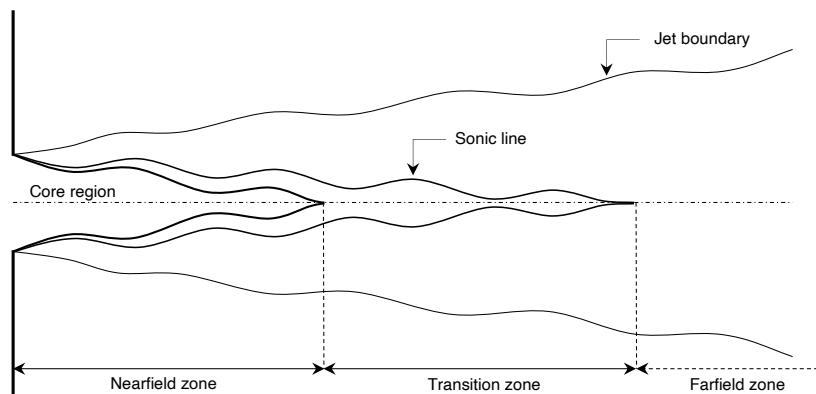


Figure 2.1: Schematic illustration of the flow field zones of an underexpanded jet.

largely considered stable. The viscous effects instead are generally assumed non relevant in this area and hence have no impact on the flow pattern. In this inner part, the fluid is initially iso-entropically expanded and then compressed again by a system of embedded compression waves that will be detailed better afterwards. On the other hand, the mixing layer, or free shear layer, is the region where the discontinuity in gas velocity at the jet edge gets smooth down [27]. This is achieved by means of viscous effects that, contrarily to what happens in the potential core, have here an important influence on the flow development. They are indeed responsible especially for the generation of instabilities that in turn, promoting entrainment from the environment, reflect on the width of the mixing layer and finally on the diameter of the jet, which grows moving downstream. The free shear layer is, then, composed of a supersonic -the inner part- and a subsonic region -the outer part- and basically consists of the transition area between the two regimes. The equilibrium at the jet edge is achieved by means of large-scale eddies, viscous effects that play the relevant role in the spreading rate and the associated decay of fluid characteristics. The behaviour is in this case dependent on the Reynolds number at the exit section. Anyway, the most often encountered case in practical situation is when $Re > 10^4$, where the mixing layer is initially turbulent and its width increases almost linearly with the distance to the exit plane [26]. Further downstream, the *transition region* and the *farfield region* -both briefly described in the following- accomplish the complete dissipation of the jet energy.

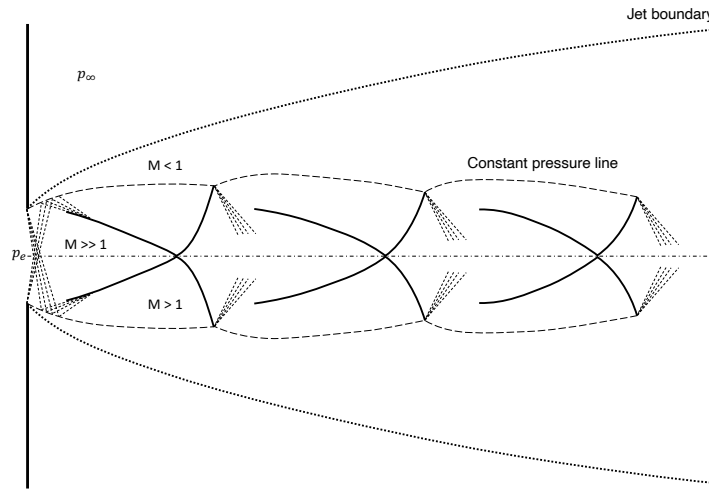


Figure 2.2: Structure of a moderately underexpanded jet.

2.3.1. Nearfield zone

The nearfield flow, as mentioned above, is governed by compressible effects and is rather steady. Here, the behaviour is primarily determined by the exit-to-ambient pressure ratio η_e , and to a lesser extent by the exit mach number and the divergence angle of the divergent section of the nozzle employed to accelerate the flow.

Depending on the nozzle pressure ratio η_0 , the supersonic jet issuing from a nozzle shows different shocks pattern, so it is in turn classified based on the stage of expansion. With growing pressure ratio, the flow is initially overexpanded, when the outlet pressure is lower than the surrounding medium; then, it becomes ideally expanded when the fluid pressure in correspondence of the outlet exactly matches the ambient one; finally, at further higher nozzle pressure ratios, the flow becomes underexpanded. In the last situation the shock pattern is commonly distinguished in *moderately underexpanded* and *highly underexpanded*. The values of pressure ratio separating these flow regimes are dependent on the physical properties of the gas issuing from the nozzle, although the variation from one gas to another is shown to be rather small.

Moderately underexpanded flow:

When the under-expansion stage is low, the jet resemble the well-known "diamond" or "X" structures, as shown in Fig. 2.2. At the exit plate the flow must suddenly expand to adapt to the external pressure P_∞ . Thus, at the device lip, a Prandtl-Meyer expansion

fan is generated to match the pressure balance at the constant pressure line (CPL), being this one the line at P_∞ which separates the subsonic and the supersonic regions of the mixing layer. The expansion waves prolong toward the jet axis, where they get reflected. The flow is then forced to cross the expansion fan once again, hence reaching a pressure lower than P_∞ . However, since the pressure balance must be always ensured at the CPL, the reflected expansion waves turn into compression waves after reaching the CPL and after getting redirected inward. In turn, the compression waves eventually coalesce to form an oblique shock which is generally known as *barrel* or *intercepting* shock. This one, subsequently, reaches the axis and get reflected radially outward, forming a new oblique shock called in this case *reflected* shock. During this process, the flow is compressed passing through the barrel shock and once again through the reflected shock, reaching a pressure greater than P_∞ . Finally, to balance again the sudden rise in pressure, the flow undergoes again an expansion process, replicating therefore the structure. This pattern continues until the viscous forces predominate sufficiently away from the nozzle exit plane. For the case of air, moderately underexpanded jets are shown to exist in a range of η_e spanning from $\simeq 1.1$ to 2.1 [10, 28].

Highly underexpanded flow:

As the pressure ratio increases (for air $\eta_e > 2.1$, [10, 29]), the regular reflection of the intercepting shock on the axis can no longer happen. This is due to the strong expansion of the jet, that causes the pressure along the axis to be too low with respect the ambient value. In this case the compression through an oblique shock would not be sufficient. Instead, the necessary strong compression takes place through a normal shock disk or *Mach disk* [30] and the ensuing flow field structure is known as *highly underexpanded flow*, schematized in Fig. 2.3.

The reflection of the intercepting shock occurs on the edge of the Mach disk, in correspondence of the point in which the three shocks (intercepting, reflected and Mach disk) meet, which is called *triple point*, forming the so-called *lambda structure*. The flow sudden downstream the Mach disk is necessarily subsonic, while supersonic flow persists in its surrounding, downstream the reflected shocks. Thus, an embedded shear layer, named *slipstream* or *slipline* forms at the interface between this two concentric domains. In other words, a slipstream is a portion of the flow that separates the flow into two segments with identical pressure and flow direction but different velocity.

When the pressure ratio is high enough, the subsonic core of the jet is quickly accelerated and becomes supersonic once again, thus replicating the structure. For further increase in pressure ratio, the flow field may instead be dominated by the presence of a unique shock cell, as shown in the Fig. 2.4. In this case, the first Mach disk has grown in both strength

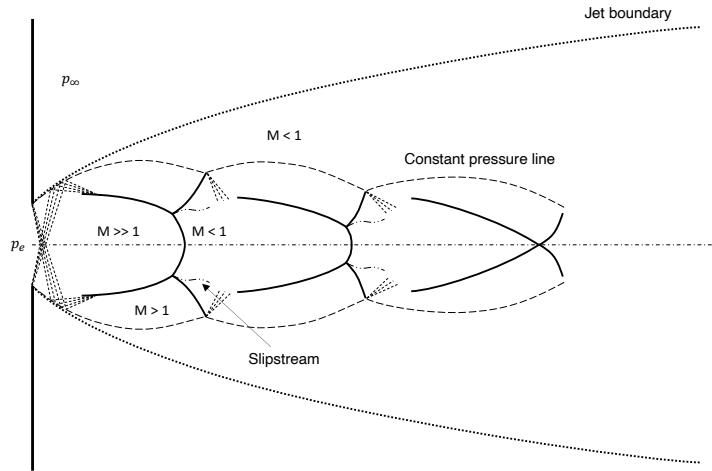


Figure 2.3: Structure of a highly underexpanded jet.

and diameter to prevent the formation of other normal shocks. In both the cases, downstream of these normal shock structures the flow then decays through a series of oblique shocks, even though such structures are distorted by the instabilities of the flow. Further downstream, these jets decelerate in the usual subsonic manner.

Overexpanded flow:

For completeness, a brief description of an overexpanded flow is here reported. This flow regime occurs every time the fluid, passing through the divergent section of the nozzle, gets expanded beyond the needed level to adapt to the external pressure. Under these circumstances, an oblique shock is formed to adjust the pressure with the external one as the flow leaves the device. The oblique shock is then reflected at the center line and crossed again by the flow, this one being hence forced through a second compression. At this stage, the fluid has then a pressure higher than the ambient value. As a consequence, the reflected shock, impacting on the jet edge, is turned in an expansion fan. The latter is subject to some reflections similar to what happens in an underexpanded jet, finally converging into an oblique shock. The shock cell is therefore repeated continuously until, even in this case, the viscous effect dissipate completely the core region. A picture of an overexpanded flow can be seen in Figure 2.5.

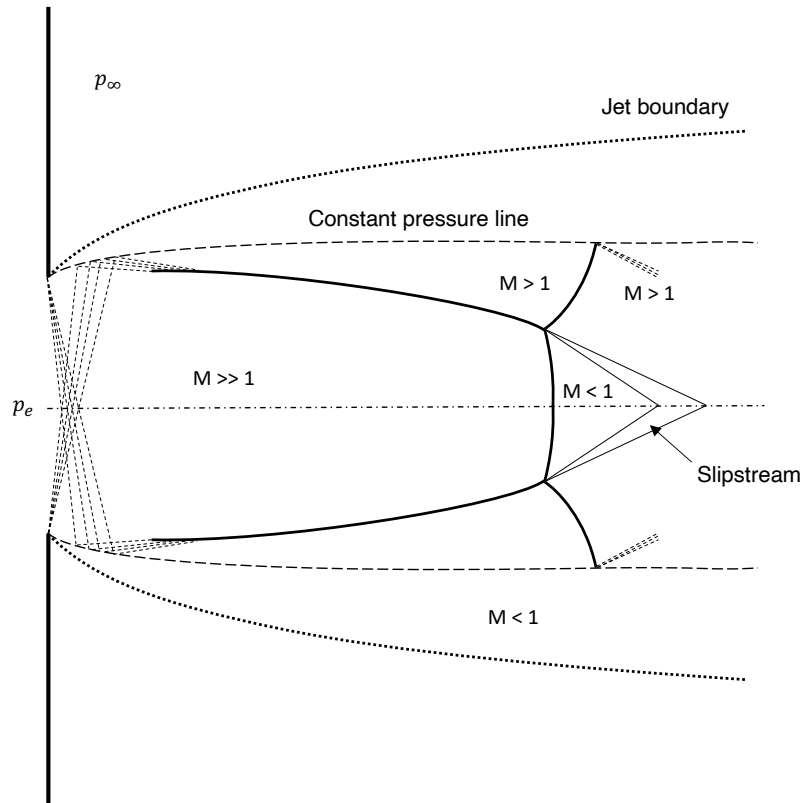


Figure 2.4: Structure of a very highly underexpanded jet.



Figure 2.5: Overexpanded jet during a SpaceX Raptor Engine Test.

2.3.2. Transition and farfield zone

The mixing layer grows during its downstream development due to the viscous effects, gradually diffusing inward and therefore reducing the energy of the core region, eventually totally replacing the inner part. When the mixing layer reaches the axis, this is said to be the beginning of the *transition region*, where the variation of the flow field characteristics are small both axially and radially and the flow field is mainly characterised by turbulence. Here, the radial diffusion is responsible to make the pressure field homogeneous, since the fluid entrainment from the external field takes place everywhere. Finally, in the *farfield region*, the flow is ideally expanded and its characteristic (mean pressure, velocity and temperature) are self-similar, i.e. the area of interest is far enough downstream so that velocity and shear stress are function of a similarity parameter. Here, the flow is considered to be fully developed. The jet is in this region considered in pressure equilibrium with the environment even though it may still have a velocity such that compressible effects cannot be neglected (i.e. $Ma > 0.3$). The velocity then decays moving farther downstream. In this case, useful information can be obtained without solving the equations of motion. Also, it has been shown analytically that the radial normalised profiles obey to the same law, which is a Gaussian. Furthermore, this area is basically not dependent on the nearfield structure, so is not important to have a detailed description of how the fluid arrived to the status it has in the farfield region.

2.4. Impinging flow structure

The typical flow structure generated by the supersonic jet impingement on a flat surface displays some relevant differences with respect to the free jet case and will be detailed in this section.

As discussed in the following, the shock pattern that can be formed is, similarly to the case of free jet, affected relevantly by the exit-to-ambient pressure ratio. However, as mentioned above, this is not sufficient to completely describe its overall structure. Indeed, the flow field is strongly influenced also by other parameters such as the Mach number in the proximity of the impinging area, the impingement angle and the nozzle-to-wall distance. Such distance is generally normalised with respect to the nozzle exit diameter. It is then impossible to classify the flow field on the basis of one parameter as has been done for a free jet. Furthermore, the flow field pattern that generates after the impingement is relevantly affected by the stage of underexpansion, i.e. moderately or highly underexpanded jet.

To identify the most important features of an underexpanded impinging jet, it is common practise to divide the flow field into three zones : the *free-jet region*, the *impingement*

region and the *radial-jet* or *wall-jet region* [5, 31, 32].

Possible schemes for a moderately and highly underexpanded impinging jets are illustrated in Fig. 2.6, where the three above-mentioned zones can be recognised.

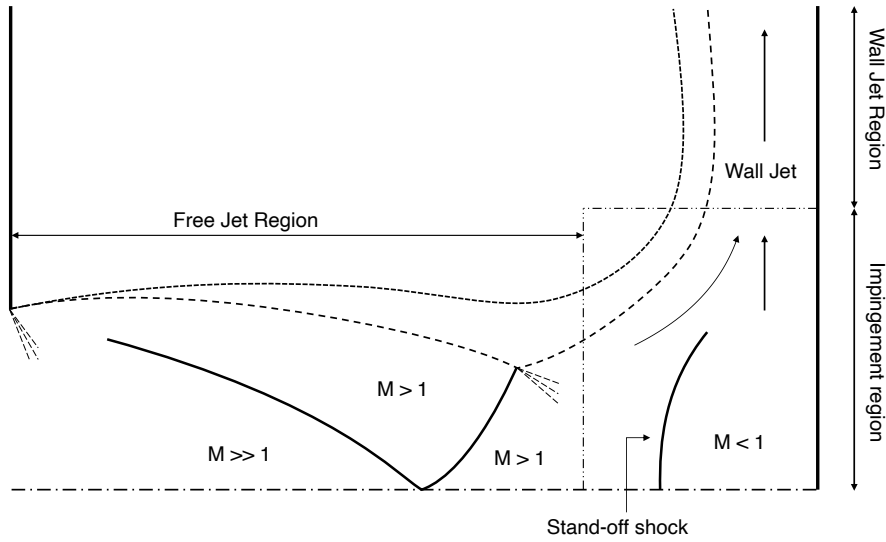
In proximity of the nozzle exit section the flow features are similar in both the free and impinging jet cases. The free-jet region structures, indeed, depend primarily on the operational conditions of the nozzle, and hence on the exit-to-ambient pressure ratio η_e . Such zone can evolve as a moderately or highly underexpanded jets and strongly influences the ensuing flow field evolution.

The flow successively impacts on the wall, forming what is known as impingement region. In this area, predominantly due to the presence of the wall, large pressure gradients exist, which force the fluid to a net change in flow direction. The interaction is in this case more or less relevant depending on the nozzle-plate distance, being more important when the potential core is closer to the impinged surface.

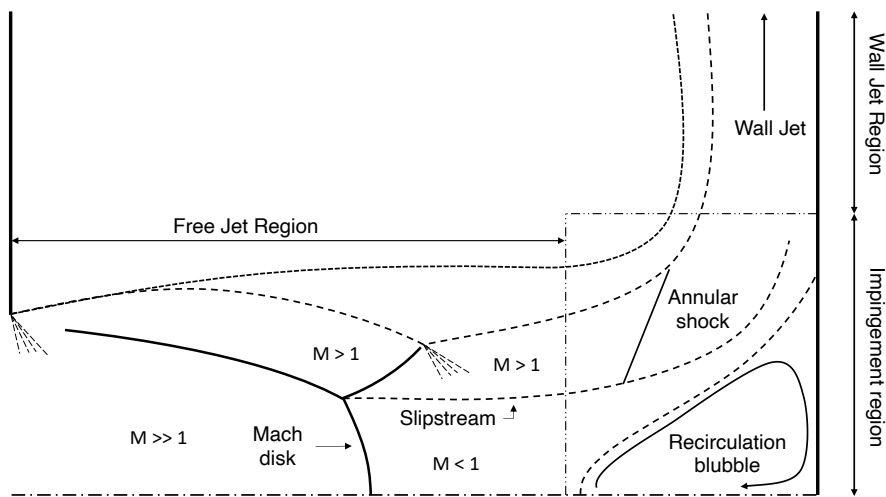
In the impingement region, a detached shock or recirculation region may form under certain Mach number condition, impingement distance and stage of underexpansion of the flow. If the flow is moderately underexpanded, the flow downstream the oblique shock reflection on the axis would be still supersonic and, if the wall is placed sufficiently close such that $M > 1$ during the impact with the surface, a detached shock orthogonal to the jet flow - the *stand-off* or *plate shock* - usually appears to meet the pressure balance close to the surface. This can lead to an off-axis peak of pressure along the plate with respect the surrounding, which consequence could be the formation of a *stagnation* or *recirculation bubble* with a conical shape in front of the plate.

Contrarily, when the shock cell close to the plate contains a Mach disk, it induces a total pressure loss higher than the one caused by the reflected shock. Downstream the normal shock the flow would then be subsonic, resulting in the absence of the stand-off shock -which is generated only if the impingement is supersonic. Nevertheless, the Mach disk introduces anyway a local total pressure loss which, once again, may lead to the presence of a recirculation region as above explained. The peak in pressure is believed to be generated by the impingement of the slipstream [19] illustrated in Figure 2.6b. As a general outcome, one may say that the presence of a strong discontinuity in proximity of the impinged wall can result in the formation of the recirculation region.

Anyway, these bubbles are shown to not significantly influence the development of the subsequent wall-jet region [12]. Although such recirculation regions have been detected in a number of studies, the conditions by which they are formed are still not entirely clear. Moreover, if a Mach disk is formed in the flow field, a slip stream separating a subsonic -behind the disk- and a surrounding supersonic region coexist, similarly to the free jet configuration. The expansion waves generated downstream the reflected shock reflect on



(a)



(b)

Figure 2.6: Moderately underexpanded (a) and highly underexpanded (b) impinging jet schemes.

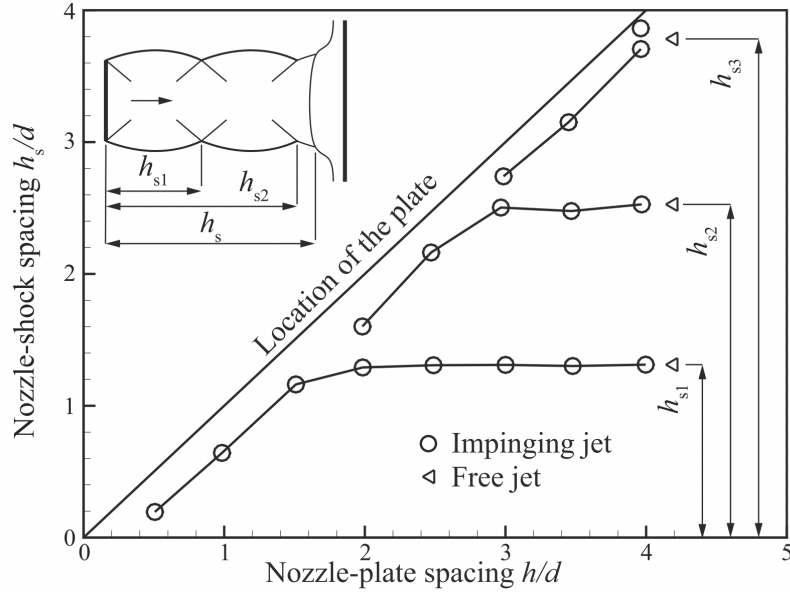


Figure 2.7: Positions of shock structures at varying impingement distances [31], where h_{s1} and h_{s2} are the distances of the reflected shock intersection with the constant pressure line and h_s is the one of the plate shock from the nozzle exit plane.

such slip line as compression waves in the supersonic flow that eventually may merge to form what is known as *annular shock* [21, 31, 33].

Additionally, although Mach disks appear in free jets only for highly underexpanded jets, they may occur at lower exit-to-ambient pressure ratio when the nozzle-to-wall distance is short enough. In this situations, the jet structure of the impinging jet at moderate and high underexpansion are rather similar and show more or less the same behavior [33]. Furthermore, it is worth mentioning that under fixed operational conditions, the length of the fully developed shock cells as well as the stand-off distance (the plate shock-to-wall distance) are shown to be insensitive to the varying impingement distance [13], as shown in Figure 2.7.

Finally, the region where the wall jet emerges is called wall jet region. The jet here moves radially outward and therefore through an expansion that causes the flow to be re-accelerated to supersonic. A trains of shock cells similar to the quasi-periodic structures in a free jet may form along the wall jet in this case. The pattern of compression and expansion in this region can endure for many jet diameters depending on the nozzle pressure ratio [12]. The wall-jet gets eventually dissipated by the viscous effects of the shear layer on the constant pressure surface of the wall jet and the boundary layer which develops along the wall. These two layers finally merge to reduce the flow at subsonic, similarly at what happens in a free jet case.

3 | Method

This chapter contains a description of the numerical method and the strategy employed to perform the analysis of the successive sections concerning both the validation and the final tests and results.

Initially, the numerical method is roughly delineated together with the descriptions of the RANS approach and the turbulence models employed in the numerical computations. Then, the numerical schemes chosen are reported. Finally, the strategy and set-up to realise the computational grid is also described.

3.1. Numerical method

3.1.1. Governing equations for compressible flow

The numerical computations contained in this work are performed making use of the open-source software SU2, a software able to solve partial differential equation on general unstructured meshes. An extensive description of the architecture of the software and V&V (verification and validation) of the code can be found at [34, 35].

In this case, the governing equations for a compressible flow are [35]:

$$\begin{cases} R(\mathbf{u}) = \frac{\partial \mathbf{u}}{\partial t} + \nabla \cdot \mathbf{F}^c - \nabla \cdot (\mu^{vk} \mathbf{F}^{vk}) = 0 & \text{in } \Omega, \quad t > 0, \\ v = \mathbf{0} & \text{on } S, \\ \partial_n T = 0 & \text{on } S, \\ (\mathbf{W})_+ = W_\infty & \text{on } \Gamma_\infty. \end{cases} \quad (3.1)$$

Where Ω is the domain of integration, S an adiabatic wall boundary and Γ_∞ the farfield boundary. In system 3.1, the first equation represent the set of PDE needed to be solved, the second and the third are respectively the the no-slip and the adiabatic condition along the solid walls, while the last one represent the farfield boundary condition.

The equations are solved for $\mathbf{u} = \{\rho, \rho \mathbf{v}, \rho e\}^T$, which is the vector containing the conservative variables, while the convective and the viscous fluxes are, respectively:

$$\mathbf{F}^c = \begin{pmatrix} \rho \mathbf{v} \\ \rho \mathbf{v} \otimes \mathbf{v} + \mathbf{I}p \\ \rho E \mathbf{v} + p \mathbf{v} \end{pmatrix}, \quad \mathbf{F}^{v1} = \begin{pmatrix} \cdot \\ \bar{\tau} \\ \bar{\tau} \mathbf{v} + c_p T \end{pmatrix} \quad (3.2)$$

where ρ is the density, \mathbf{v} is the velocity vector, E the total energy per unit mass, p the static pressure, c_p is the specific heat at constant pressure and T is the static temperature of the fluid. The fluid is modeled as perfect gas, hence the constitutive equations are:

$$p = \rho R T, \quad e = c_v T, \quad h = c_p T, \quad (3.3)$$

being R the specific gas constant, c_v the specific heat at constant volume and h the specific enthalpy.

Additionally, $\bar{\tau}$ is the viscous stress tensor, defined as:

$$\bar{\tau} = \mu(\nabla \mathbf{v} + \nabla \mathbf{v}^T) - \frac{2}{3}\mu \mathbf{I}(\nabla \cdot \mathbf{v}). \quad (3.4)$$

where μ is the viscosity of the fluid, which is modeled by the Sutherland's law [36].

3.1.2. RANS approach

When turbulent flows are considered, the simulations must be solved exploiting the well-known Reynold-Averaged Navier-Stokes (RANS) approach. These equations are time-averaged Navier-Stokes (NS) where, on the basis of the Favre decomposition, the instantaneous velocities and temperatures are split in their density weighted average \tilde{u} and a fluctuation around that value u'' . Using the simple average \bar{q} , one defines the density weighted average as

$$\tilde{q} = \frac{\bar{\rho q}}{\bar{\rho}} \quad (3.5)$$

Hence, the RANS equations are:

$$\frac{\partial}{\partial x_j}(\bar{\rho} \tilde{u}_i \tilde{u}_j) = -\frac{\partial \bar{p}}{\partial x_i} + \frac{\partial}{\partial x_j} \left[\mu \left(\frac{\partial \tilde{u}_i}{\partial x_j} + \frac{\partial \tilde{u}_j}{\partial x_i} - \frac{2}{3} \frac{\partial \tilde{u}_l}{\partial x_l} \delta_{ij} \right) \right] + \frac{\partial}{\partial x_j} (-\overline{\rho u''_i u''_j}), \quad (3.6)$$

being \tilde{u}_i the density weighted average of u in the i -direction and u''_i its fluctuation [37]. The time-averaging of the complete NS generates therefore an additional term $\overline{\rho u''_i u''_j}$ which is known as *Reynold stress tensor (RST)*, that needs to be appropriately modeled - by

turbulence models - for the closure of the problem. There are several models available in literature. An exhaustive list and description can be found at [38].

In most cases, the Reynolds term is defined on the basis of the Boussinesq assumption, which relates the *RST* to the mean-flow strain tensor S by means of the *turbulent* or *eddy viscosity* μ_t , being this one an additional term to the dynamic viscosity μ_d of the fluid. The Boussinesq assumption then gives [39] :

$$-\overline{\rho u''_i u''_j} \hat{=} \mu_t \left(\frac{\partial \tilde{u}_i}{\partial x_j} + \frac{\partial \tilde{u}_j}{\partial x_i} - \frac{2}{3} \frac{\partial \tilde{u}_k}{\partial x_k} \delta_{ij} \right) - \frac{2}{3} \bar{\rho} \kappa \delta_{ij}, \quad (3.7)$$

where κ is the turbulent kinetic energy (TKE), needed for two-equations turbulence model. The turbulent viscosity is an additional unknown quantity and, in turn, need to be modeled by means of one or more transport equations. Models based on Eq. 3.7 are generally referred as *Eddy viscosity models (EVM)*.

Alternatively, the Reynolds stress can be also more generally modeled by *Reynolds stress models (RSM)*, which either solve new separate transport equations per each component of the *RST*. An intermediate approach are *Explicit Algebraic RSM (EARSM)* which provide a more elaborate modeling of the RST on the basis of flow conditions and 2 turbulence transport equations. The RSM approach is nevertheless not often used in the industry so far.

In the context of this work, the choice of the turbulence model is relevant not only for the overall properties of the flow field, but also on the reliability of the numerical solution. Indeed shocks may have an impact on the production of the eddy viscosity, which would be non-physical.

Two of the most widely used EVM turbulence models in this kind of applications are the standard *Spalart-Allmaras (SA)* [40] and the *Shear Stress Transport by Menter (SST)* [41]. Both of them are available in SU2 and briefly described in the following.

The Spalart-Allmaras model (SA):

The Spalart-Allmaras model is the most simple EVM as it only consists on solving a single transport equation for the turbulent viscosity μ_t . For this reason, it is generally referred to as a one-equation model. The SA has been successfully applied to external aerodynamic flows in many applications. On the other hand, it could result to be too simple and can leads to not accurate results. While in this section only a rough description is provided, the full treatise of the model can be found at [40, 42]. The transport equation is in this

case solved for the turbulent kinematic viscosity $\hat{\nu}$ and is:

$$\begin{aligned} \frac{\partial \hat{\nu}}{\partial t} + u_j \frac{\partial \hat{\nu}}{\partial x_j} = c_{b1}(1 - f_{t2})\hat{S}\hat{\nu} - \left[c_{w1}f_w - \frac{c_{b1}}{\kappa^2}f_{t2} \right] \left(\frac{\hat{\nu}}{d} \right)^2 \\ + \frac{1}{\sigma} \left[\frac{\partial}{\partial x_j} \left((\nu + \hat{\nu}) \frac{\partial \hat{\nu}}{\partial x_j} \right) + c_{b2} \frac{\partial \hat{\nu}}{\partial x_i} \frac{\partial \hat{\nu}}{\partial x_i} \right], \end{aligned} \quad (3.8)$$

needed to compute the eddy viscosity as $\mu_t = \rho \hat{\nu} f_{v1}$, where

$$f_{v1} = \frac{\chi^3}{\chi^3 + C_{\nu 1}^3}, \quad \chi = \frac{\hat{\nu}}{\nu}, \quad \nu = \frac{\mu_d}{\rho}. \quad (3.9)$$

The terms c_{bi} , c_{w1} , f_w , f_{t2} present in Eq. 3.8 are constant and are not here reported.

The production term \hat{S} is defined as

$$\hat{S} = \Omega + \frac{\hat{\nu}}{\kappa^2 d^2} f_{v2} \quad (3.10)$$

where d is the distance to the nearest wall, κ a constant and $\Omega = \sqrt{2W_{ij}W_{ij}}$ is the magnitude of the vorticity, being

$$W_{ij} = \frac{1}{2} \left(\frac{\partial u_i}{\partial x_j} - \frac{\partial u_j}{\partial x_i} \right). \quad (3.11)$$

Hence, the turbulent viscosity is generated by the presence of vorticity, thus any time viscosity effects are produced, such as in boundary layers or shear layers; but not in shocks. Additionally, the SA has a non-zero source term also in the free-stream, even when the vorticity is zero. Despite this, its dependence decays with $1/d^2$.

The imposed boundary conditions are such that there is no production of turbulent viscosity at the wall, while its farfield value is typically chosen as a fraction of the corresponding laminar quantity.

Finally, should be recall that the formulation presented here is the original SA model, referred as *standard* [42]. However, further improvements of this work can account for a compressible correction available for the SA model which refines the flow behavior in the mixing layer. This is accomplished by including an additional term on the right side of the equation which depends on the local speed of sound a [43]. Anyway, the SA standard version is still applicable for both incompressible and compressible flows [44], in particular for lower values of TKE.

The Menter Shear Stress Transport model (SST):

The SST is instead an eddy viscosity two-equation model. The variant here reported is the version formulated by Menter [41] of the standard $\kappa - \omega$ model. The turbulent viscosity is in this case modeled by means of two transport equation: one for the *turbulent kinetic energy* κ and the other for the *specific dissipation rate* ω . The SST is commonly used for applications such as turbulent round jets, and in many applications has shown better performances with respect to the SA in terms of physics prediction and numerical robustness [37, 45].

In this case, the governing equations are [46]:

$$\begin{cases} \frac{\partial(\bar{\rho}\kappa)}{\partial t} + \frac{\partial(\bar{\rho}\tilde{u}_j\kappa)}{\partial x_j} = P - \beta^*\bar{\rho}\omega\kappa + \frac{\partial}{\partial x_j} \left[(\mu + \sigma_k\mu_t) \frac{\partial\kappa}{\partial x_j} \right], \\ \frac{\partial(\bar{\rho}\omega)}{\partial t} + \frac{\partial(\bar{\rho}\tilde{u}_j\omega)}{\partial x_j} = \frac{\gamma}{\nu_t}P - \beta\bar{\rho}\omega^2 + \frac{\partial}{\partial x_j} \left[(\mu + \sigma_\omega\mu_t) \frac{\partial\omega}{\partial x_j} \right] + 2(1 - F_1) \frac{\bar{\rho}\sigma_{\omega 2}}{\omega} \frac{\partial\kappa}{\partial x_j} \frac{\partial\omega}{\partial x_j}, \end{cases} \quad (3.12)$$

where

$$P = \tau_{ij} \frac{\partial u_i}{\partial x_j} \quad (3.13)$$

and constants all the other quantities which are not reported here but can be found at [46]. The eddy viscosity is this time computed as:

$$\mu_t = \frac{\bar{\rho}a_1\kappa}{\max(a_1\omega, \|\mathbf{w}\|F_2)}. \quad (3.14)$$

The SST source terms depend, other than on the vorticity, also on the velocity gradient in a non-direct manner. Indeed, the production term P contains the viscous shear stress tensor, that in turn depend on the gradient of the velocity. In particular, in presence of velocity gradient the SST produces turbulent viscosity. Also (isolated) shocks generate turbulence whereas in real conditions they should not. This sensitivity to the velocity gradient can hence have an impact on the flow field and negatively influence the solution. Regarding the boundary conditions for the transport equations 3.12, the value of κ must be zero and the value of ω is set to be constant on the walls. On the farfield instead the value of κ has to be contained among two constants defined by a Reynolds number related to the laminar viscosity and the free-stream velocity, and the same is true for the value of

the dissipation rate ω . The idea is that the turbulent viscosity at the farfield must have a value much smaller than the one of the free-stream laminar viscosity (among 1E-02 and 1E-05).

A relevant issue related with this models is the non-physical decay (sometimes dramatic) of the turbulence variables from their set values in the farfield for external aerodynamic problems. This problem can be solved by the *SST_SUST* [47] version of the SST which eliminates the non-physical decay in the free-stream through the addition of sustaining terms to the equations. Nevertheless, also the SA shows similar performances in predicting the decay of characteristics in turbulent round jets.

3.2. Numerics

SU2 provides the possibility to solve an axisymmetric three-dimensional problem on a two-dimensional grid by exploiting its in-built axisymmetric solver. This feature allows a dramatic reduction in the number of cells - and consequently the run-time - that would be required to complete a fully three-dimensional simulation.

The axisymmetric solver necessitate the definition of an axis of symmetry, which is defined by setting the corresponding boundary condition. In this context, it is the bottom edge of the domain, being this one the center line of the flow.

In all the simulations, the fluid is modelled as perfect gas and the Sutherland's law [36] is used for the estimation of the dynamical viscosity μ_d .

The numerical method is a *Finite Volume Method (FVM)* with reconstruction of gradient. Concerning the numerical schemes, the *Roe Riemann solver (ROE)* has been adopted for the integration of the convective fluxes while the gradients of the flow variables are computed using the *Green-Gauss* method. Second-order accuracy is achieved via reconstruction of variables on the cell interfaces by using a *Monotone Upstream-centered Schemes for Conservation Laws (MUSCL)* approach. Since flow discontinuities are physically expected during a supersonic expansion, a gradient limiter, such as the the Barth et. Jespersen [48] or the Venkatakrisnan [49], is required to prevent spurious oscillations across those discontinuities. The application of the limiter is case-dependent. The former has been initially preferred because of its accuracy. However, in some cases it failed to reach convergence due to its non-differentiability (no smooth transition between limiting and not limiting). Hence, the latter has been employed, providing this one better overall convergence [50].

The system is solved using an damped inexact Newton iteration, which solves, using a

Newton iteration, the implicit pseudo-time integration

$$\frac{u^{n+1} - u^n}{\Delta\tau} + Res(u^{n+1}) = 0 \quad (3.15)$$

with the pseudo time step $\Delta\tau$ determined by the *Courant-Friedrichs-Lax (CFL)* number:

$$\Delta\tau = \frac{CFL \Delta x}{u}, \quad (3.16)$$

where Δx is a local characteristic length for the cell. For stability reasons, the solver is generally initiated with a small CFL, which increases as the method converges. Consequently, the pseudo time step increases and the method gradually switches to a pure newtonian one. The maximum CFL number hence depends on the convergence performance of the specific simulation.

The corresponding linear system is solved using the *Flexible Generalized Minimal Residual (FMGRES)* method with high linear solver iteration (100) to improve the accuracy of the solution. The turbulence model employed are the SA and the SST models (together with its alternative version SST_SUST). A scalar upwind method is a standard choice for the turbulent convective fluxes and has been employed even in this case. No reconstruction is used concerning the turbulence solution.

Finally, the convergence criterion is based on the residual of the density and is fulfilled when it reaches the value of 10^{-11} .

3.3. Mesh set-up

The numerical grids employed to perform all the simulations described further on have been realised making use of the mesh-generator software Gmsh [51]. The meshes are two-dimensional and unstructured and consist of the assembly of the nozzle and the open boundary in all the cases. Taking advantage of the axis-symmetry of the problem, only half of the domain has been modeled.

A finer grid is employed at the nozzle throat and across the zones where stronger gradient are expected, i.e. the region of free expansion of the jet and, in case of impingement, above the wall of the impinged surface. Refinement boxes are useful for this purpose and have been exploited. The mesh becomes then gradually coarser with rising distance from the axis. Furthermore, an additional local refinement is considered whether boundary layers have to be computed, i.e. on the internal wall of the nozzle and over the flat plate in case of impinging jet. The thickness of the first cell corresponding to such wall mesh is in all the cases chosen in order to ensure that the value of the dimensionless wall coordinate $y+$

[52] is sufficiently small to avoid numerical instabilities. The mesh algorithm employed is the *Frontal-Delaunay* for 2D meshes.

The domain size changes from case to case. As a general criteria, the axial extension is such that the supersonic core is always totally contained into the computational space in order to avoid instabilities related to blended subsonic and supersonic outlet in correspondence of the outlet boundary (which is always the right boundary in the numerical computations contained in this work).

A parameter h is used to parameterise the spacing among cells and suitable multiplication factors are used to scale the value of h and, hence, to set the actual size of the cells within the domain. In this way the mesh refinement can be varied by simply adjusting the parameter h , which actually represents the average size of the cells at the nozzle exit section and in the refinement boxes.

In order to obtain numerical results which are independent on the mesh refinement, a grid independence analysis was performed. This is however compulsory in order to validate the code. Object of this study is to define the lowest refinement that the mesh can have, provided that it ensures the most accurate results.

The grid independence analysis has been achieved taking as reference the experimental results obtained by Troutt and McLaughlin [53] and has been performed following the hereafter described strategy. Firstly, the most suitable value of h is found concerning the free flow set-up. This has been accomplished by progressively lowering the value of h until the results predicted by two different refinements were enough similar. Indeed, as the grid is refined (cells become smaller and the number of cells in the flow domain increases), the spatial discretization error should asymptotically approaches zero. Then, in order to assess if the chosen grid was sufficiently fine for all the simulations, the same criterion -considering the three lower values of h - has been applied also in case of flow issuing on a flat plate. In this case, the nozzle-to-wall distance has been arbitrarily chosen to be $z/D = 6$.

Finally, to preserve the same mesh quality in cases of different nozzle size, the value of h has been scaled on the basis of the ratio between the two throat diameters.

The results of this analysis are discussed in the next chapter.

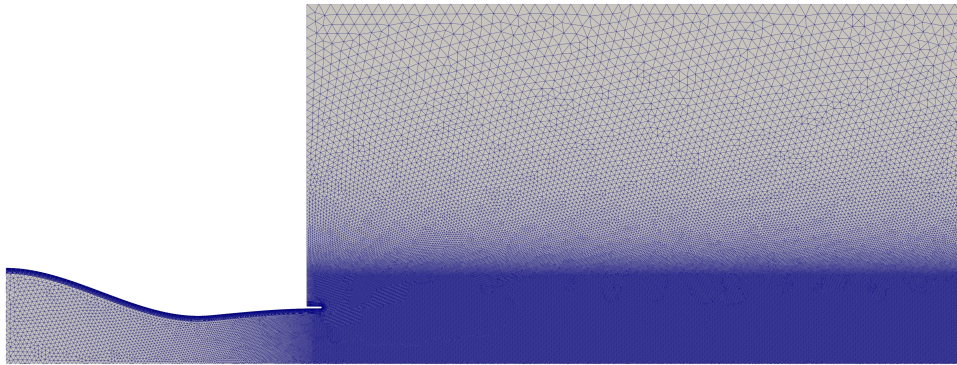


Figure 3.1: Magnification of the nozzle region of the computational grid used in case of supersonic jet released in a free environment, where a refinement box can be seen downstream of the nozzle and the wall-mesh on its internal wall.

4 | Verification and validation

This chapter deals with the verification and validation of the computations, which objective is to demonstrate the accuracy of CFD simulations in predicting the real world physics. Verification corresponds to checking whether the equations are properly solved, whereas validation concerns the comparison to the real-life data. The credibility of data extrapolated from simulations can be obtained by demonstrating acceptable levels of uncertainty and error, which refers to the level of agreement with physical reality.

By doing so, further simulations data can be used to predict phenomena with a sufficient level of confidence, even in absence of experimental data [54].

Since the equations are supposed to be correctly implemented, verification consists in this work in proving simulation independence from the grid. Validation is done by checking the agreement with real experimental data available in literature. Following the example of Chin et. al. [20], this analysis has been carried out for both underexpanded jet released in a free environment and impacting on a flat plate. By replicating their procedure, potential set-up errors can be detected and, if needed, corrected.

The turbulence models uncertainties have been also assessed by comparing the performances of the Spalart-Allmaras (SA), the Shear Stress Transport (SST) by Menter and its SST_SUST variant, as successively discussed.

This chapter is composed of two section: (i) validation of the free flow case; (ii) validation of the impinging flow case. Both the cases are initially described. Then, the results obtained are discussed. Finally, some comment on the uncertainties of the simulation are reported.

4.1. Free flow validation

4.1.1. Case description

The chosen reference for validating the code in case of a free jet are the experimental measurements performed by Troutt and McLaughlin [53], which investigated the flow field and acoustic properties of a moderately underexpanded jet. An axisymmetric convergent-

divergent nozzle with an outer diameter D_e of 10mm was used to accelerate an air flow to $M = 2$ exhausting in a low-pressure test chamber ($p_\infty = 5000Pa$). The throat diameter was $D_t \simeq 7.7$ mm and the area ratio $A_e/A^* \simeq 1.6875$. During their tests, the centre-line Mach number distribution and radial Mach-number profiles of four axial location have been measured and will be here taken as reference to assess the accuracy of the code.

The nozzle contour has been designed using the method of characteristics. Since the exact profile was not reported in literature, the contour has been defined by exploiting a Matlab[®] code which implements a two-dimensional method of characteristics. In this manner, the contour of the diverging section of a 2D nozzle having area ratio equal to the root mean square of the actual one was obtained. This method is apparently accurate enough to detect the proper flow evolution throughout the device and is discussed in the next section.

The computational parameters used during the numerical simulation are summarized in 4.1 and are chosen in a way such that the results can be compared with those obtained by Chin et. al.; similarly, the dimension of the computational domain are set to be the same as the reference. The diameter of the nozzle is instead decided after the one selected by Troutt and McLaughlin in their tests. For the sake of clarity, henceforward the numerical reference will be indicated as NR and the experimental reference of Troutt and McLaughlin as TM .

The Reynolds number based on the TM nozzle exit conditions is evaluated based upon a hypothetical isentropic expansion and the Sutherland's law [36] to compute the dynamic viscosity and results to be $Re_e \simeq 5 \times 10^4$ ¹. In particular, it is computed as:

$$Re = \frac{\rho u D_{ext}}{\mu}. \quad (4.1)$$

To explore the turbulence model uncertainties and to investigate their performances in simulating this kind of flows, the same computation was performed multiple times with the only difference being the turbulence model.

The computational domain employed in this phase is reported in Figure 4.1, together with the chosen boundary conditions (BC).

¹The Re reported by TM is actually $\simeq 70.000$. Nevertheless, it has been recomputed in this work and results to have a different value.

M_e	Re_e	P_∞	P_e/P_∞	T_0	T_e/T_∞	D_e	A_e/A^*
2	5×10^4	5000Pa	1.03	294K	0.55	10mm	1.6875

Table 4.1: Computational parameters in case of free jet.

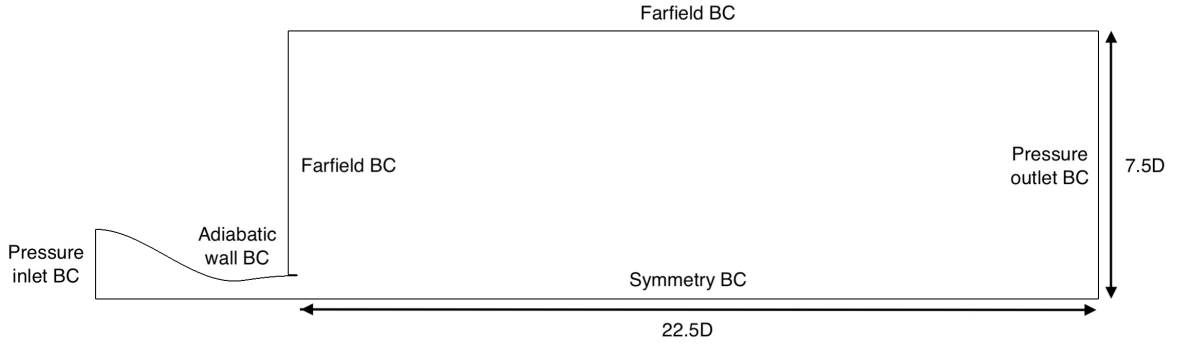


Figure 4.1: Computational domain and boundary conditions used to validate the free flow case.

In particular, the thermodynamic conditions employed in this case are:

- $P_0 = 40296Pa$, $T_0 = 294K$ and $u = (1, 0, 0)$ m/s for the inlet of the nozzle;
- no-slip condition for the adiabatic wall of the nozzle with no heat-flux;
- $P_\infty = 5000Pa$, $T_\infty = 294K$ and $Ma_\infty = 0.01$ for the farfield BC² ;
- $P_\infty = 5000Pa$ for the right boundary of the domain;

Finally, the symmetric boundary condition is required for the axisymmetric solver to identify the axis of symmetry, as previously mentioned.

4.1.2. Grid independence analysis

In order to obtain reliable results, the independence from the grid refinement has to be proven. This is accomplished following the strategy described in 3.3.

Tab. 4.2 contains the values of the parameter h and the corresponding number of cells.

²The imposition of $Ma_\infty \neq 0$ is due to computational stability reasons. The farfield Mach number should in theory be identically zero.

	mesh1	mesh2	mesh3	mesh4	mesh5
spacing h	2e-04	1.5e-04	1e-04	6.5e-05	5.5e-05
n° of cells	142.576	249.426	560.073	967.389	1.521.301

Table 4.2: Values of h and respective number of cells.

The result in case of free jet are shown in Figure 4.2, where the axial evolution of the Mach number is reported for different mesh refinements. In the graph, $z/D = 0$ corresponds to the nozzle exit section. The results predicted by all the meshes apparently compare well concerning the central region of the flow field, with the exception of *mesh1*. Despite this, the lower quality grids are evidently unable to accurately catch the oscillation due to the first shock reflection on the axis ($z/D \simeq 1$), as magnified in the graph. Also, the Mach number decay in the farfield region changes as the mesh is refined.

From the investigation of the results, *mesh4* and *mesh5* finally predict sufficiently close outcomes both concerning the oscillating region close to the nozzle outlet and the successive decreasing trend.

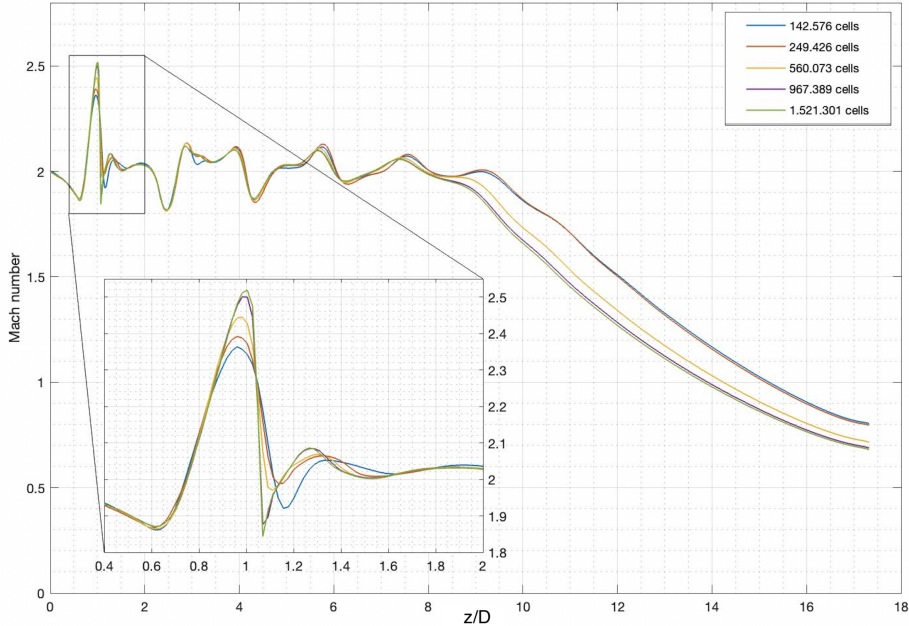


Figure 4.2: Axial Mach number per different mesh refinements - Free flow case.

The grid employed for the following analysis is finally illustrated in Figure 4.3.

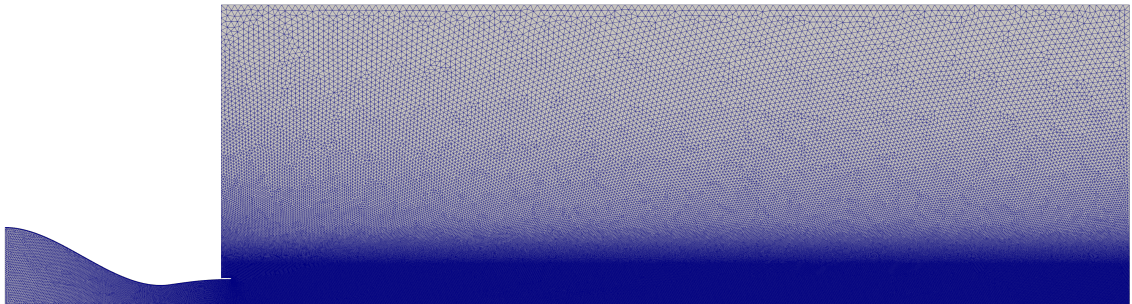


Figure 4.3: *mesh₄* used for validating the free flow.

4.1.3. Results

To assess the consistency of the numerical method with respect to the expected outcomes, the conditions at the outlet of the nozzle are firstly inspected for the SA turbulence model (coincident results are obtained for the SST). The Mach number and pressure radial distributions are reported in Figure 4.4.

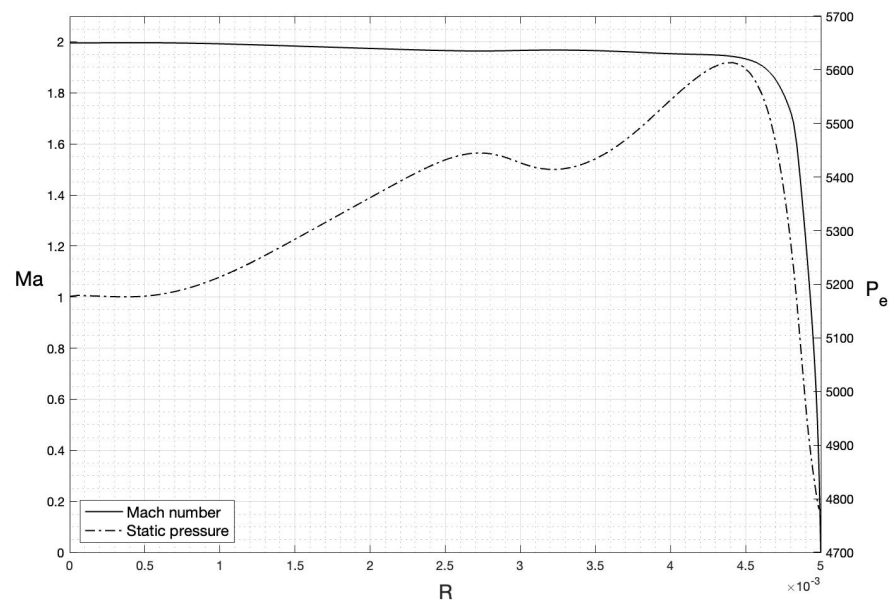


Figure 4.4: Mach Number and Static Pressure distribution along the outlet corresponding to the nozzle used in [53]

The former, accordingly to the expectations, is $Ma = 2$ and uniform across almost the whole outlet, with the exception of the region close to the wall where a boundary layer

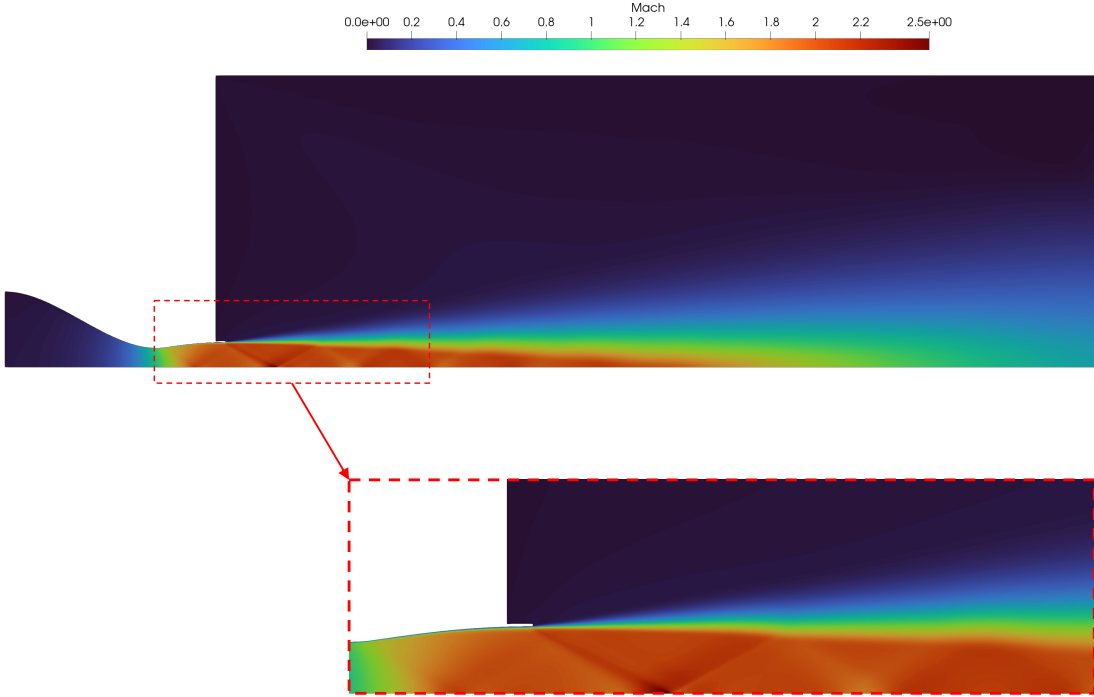


Figure 4.5: Colour plot of the Mach number field obtained replicating numerically the experimental set-up of Troutt and McLaughlin [53] with magnification of the nozzle outlet region.

is formed. On the other hand, the static pressure distribution is non-homogeneous and its value along the axis is $P_{ax} = 5177.4Pa$, slightly above the value predicted in the NR ($P_{ax_NR} = 5150Pa$). The Reynolds number based on the average conditions across the outlet has been also computed and is $Re \simeq 5 \times 10^4$ even in this case. The geometry of the nozzle obtained with the two-dimensional characteristics lines theory then can be considered suitable and was hence used to perform the ensuing simulations.

In Figure 4.5 the colour plot of the Mach number is illustrated. The flow resembles the moderately underexpanded jet pattern with regular reflections of the intercepting shocks over the centre-line, accordingly with the range of underexpansion stage discussed in 2.3, being $\eta_e = 1.03$. The maximum Mach number is $Ma \simeq 2.5$ and is reached along the axis, before the reflection of the first intercepting shock.

Figure 4.6 reports the outcomes obtained with different turbulence models, compared with those of NR (SST turbulence model) and the experimental measurements of TM. All the numerical results apparently compare well with each others, but show some divergence with the experimental data. In first place, worth noting how all the numerical computations predict wide oscillations in centre-line Mach number in the nearfield region. This

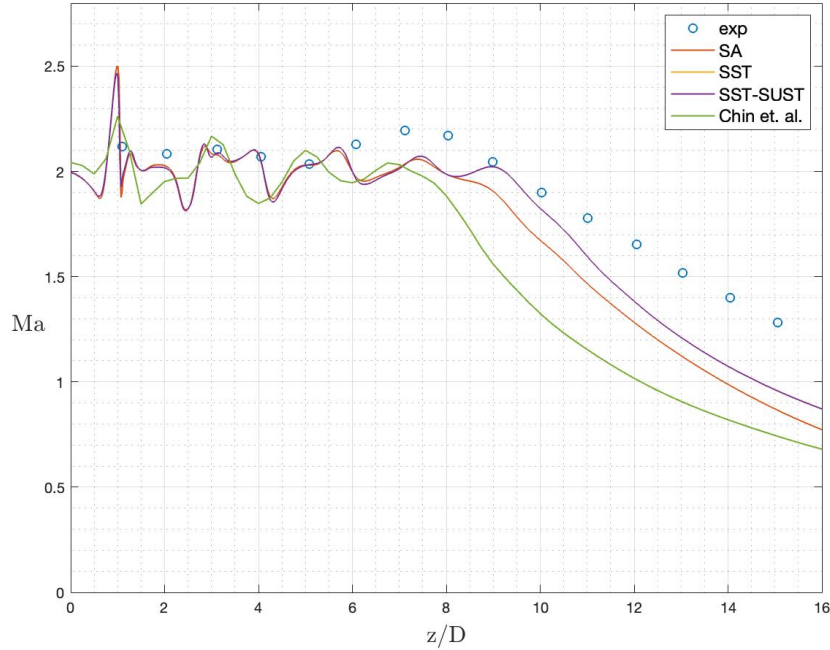


Figure 4.6: Axial Mach number per different turbulence models compared with the results of [20].

is due to the periodic diamonds structures that form in a moderately underexpanded jet, caused by alternating compressions and expansions needed for the alignment of the flow. Additionally, the axisymmetric SU2 set-up predicts higher peak in velocity along the axis compared to NR. Should be noted at this point that the SA and both the versions of the SST predict almost the same behavior concerning the core region. In particular the SST and the SST_SUST results differ negligibly and completely overlap in the graph, unless extensively magnified. Hence, the former will not be considered from now on.

Furthermore, the RANS approach predicts a flow evolution substantially different from reality far from the nozzle exit. This can be reconducted to the non-physical decay of the fluid characteristics which is intrinsic in the turbulence models and has been mentioned in 3.1.2. However, the here computed simulations provide better results compared to NR approximately for $z/D > 7$, although still not accurate enough for higher distances. Referring to the results as yet obtained, one can say that the SST provides better overall performances, being the error in predicting the velocity lower for distances approximately $z/D > 8$. Additionally, it has been noted the SST is in general more stiff to converge with respect to the SA.

Successively, the Mach number profiles in the radial direction are represented for four different axial locations and reported in Figure 4.7. The axial locations, illustrated

Figure 4.8, are selected in order to compare the plot with the data of TM and are $z/D = [1, 5, 10, 15]$. The performances of the SA and the SST are even in this case compared.

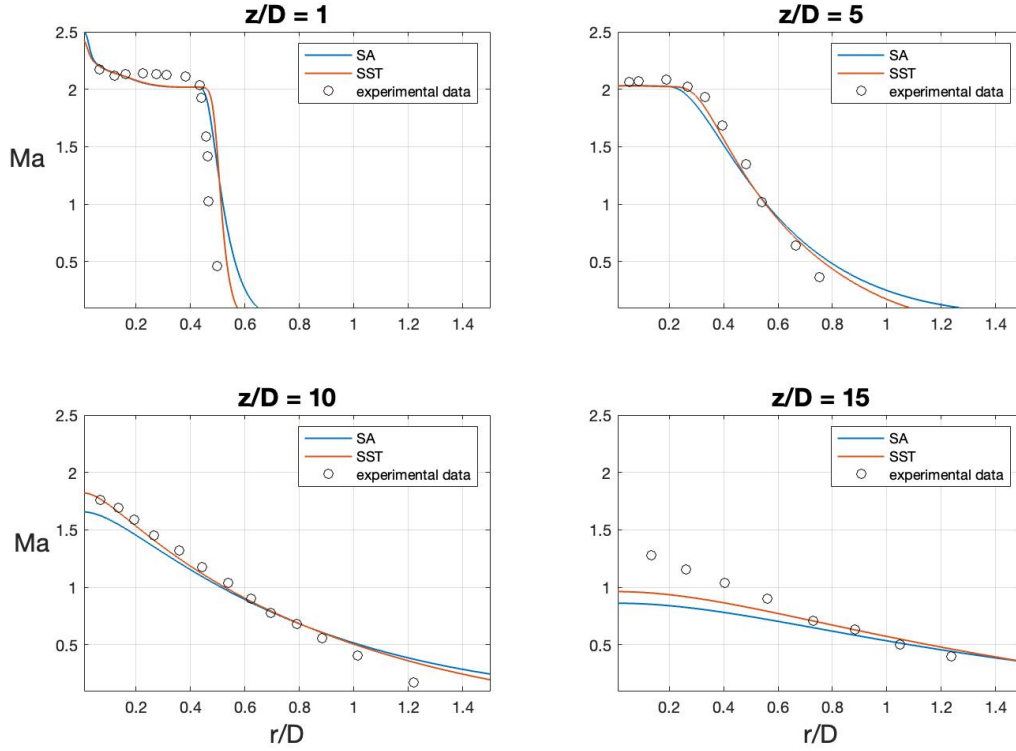


Figure 4.7: Comparison of the streamwise Mach number profiles in the radial direction at different axial location obtained with different turbulence models. The results are compared with the experimental data reported in Troutt and McLaughlin [53]. (a) $z/D = 1$, (b) $z/D = 5$, (c) $z/D = 10$, and (d) $z/D = 15$.

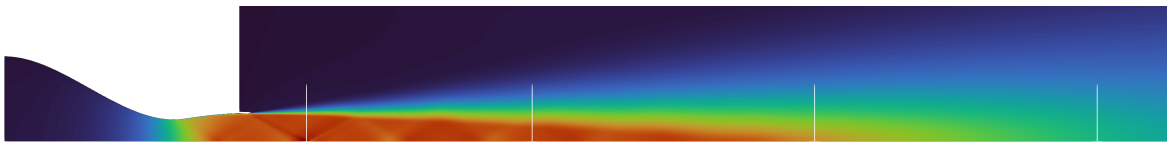


Figure 4.8: Axial location of the plots reported in Figure 4.7.

The numerical results are shown to match almost completely for small distances from the nozzle exit, confirming that the evolution of core region is correctly predicted by both the turbulence models. The peak in velocity along the axis depicted at $z/D = 1$ is due to the location of the first plot being coincident with the reflection of the first intercepting

shock.

With rising distances, the spreading of the velocity along the radial direction becomes more preeminent, consequence of the shear layer development on the outer area of the jet. In this case, the numerical results compare well with the experimental data up to $z/D = 10$, while afterwards the radial Mach number is considerably underestimated. This is coherent with what has been said above, regarding the spreading of the velocity caused by the turbulence models. Similar profiles are also detected by Chin. et. al., confirming that the error is systematic and not attributable to the here employed numerical set-up.

4.1.4. Numerical Uncertainties

Is worth to notice that some numerical uncertainties have been acknowledged during the post-processing phase and are here reported.

In first place, the turbulent viscosity is correctly generated by the turbulence models along the shear layer and then transported downstream. However, it experiences an unusual generation towards the outlet of the domain irrespective to the turbulence model, as illustrated in Figure 4.9. This represent a numerical uncertainties as the only turbulence source physically expected along the whole domain is the shear layer, being the one in analysis a free-jet case. An additional simulation with more strict convergence criteria has been performed to confirm the convergence of the results reported, bringing the residuals of the equations to further lower values (-16 for the density equation and -11 for the energy equation, in logarithmic scale). In spite of this, the solution appear to be perfectly coincident with the previous one, verifying the convergence.

This may suggest that the solution predicted by the RANS approach is not completely compatible with the superimposition of the boundary conditions. Is here anticipated that the eddy viscosity is similarly generated toward the end of the domain in almost all the simulation of this work, both for the free-jet and impinging jet. Indeed, the turbulent viscosity iso-lines always behave oddly in correspondence of the outlet boundary, indicating that some interaction is taking place. Although this, this issue takes place in an area far from the region of interest and hence has not be considered decisive.

Secondarily, as further confirm of what explained above, the static pressure across the outlet of the domain (right boundary) results wrongly imposed with respect to the boundary condition. Indeed, the flow field experiences a slightly lower pressure ($P = 4918.11Pa$ on the axis) with respect the imposed boundary value ($P = 5000Pa$). This may also affects marginally the stage of underexpansion in case of free jet, resulting in a exit-to-ambient pressure ratio higher than the actual imposed value.

Finally, even though some uncertainties are present in the numerical results, the overall

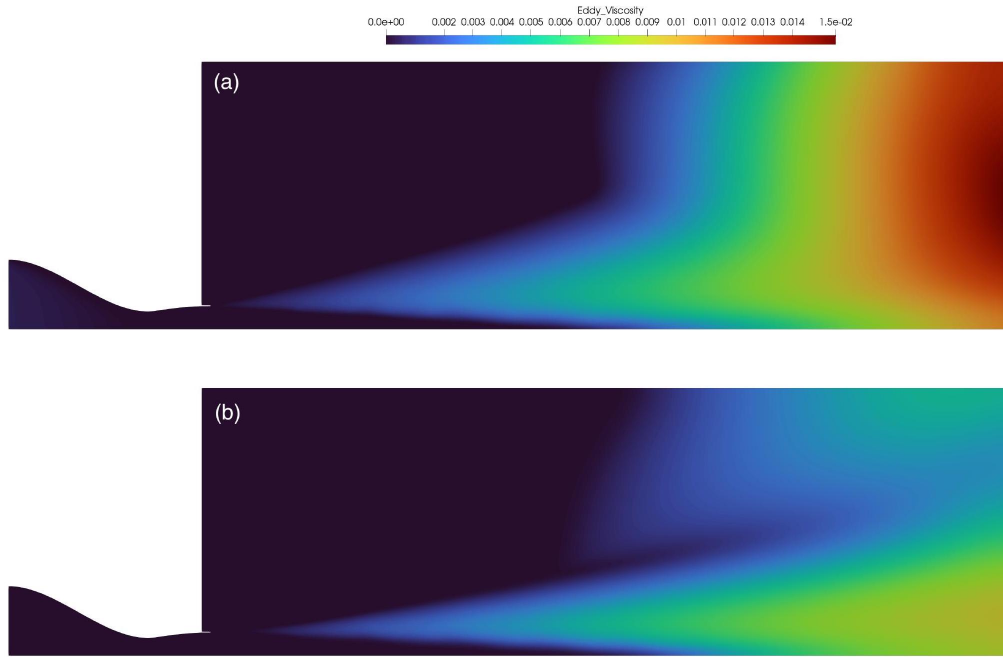


Figure 4.9: Colour plot of the eddy viscosity in case of SA (a) and SST (b) turbulence model.

quality of the simulations was judged sufficient to numerically replicate an underexpanded jet expanding in an open space, particularly concerning the core region evolution - which is the focus of this work.

4.2. Impinging flow validation

4.2.1. Case description

Next, the code must be validated even in case of supersonic impinging jet. With this regard, the real data reference is the experimental study conducted by Donaldson and Snedeker [10] (indicated as *DS* hereafter). In their tests, they employed a purely convergent nozzle and measured the pressure distribution generated by the impingement over a flat plate of height $P \simeq 9D$, varying the nozzle-to-wall distance and grade of underexpansions, this one spanning from moderately to highly underexpanded.

In this work, only the highly underexpanded jet will be taken into account, which has an exit-to-ambient pressure ratio of $\eta_e = 3.57$. In this way, the code validation will also cover the case in which a Mach disk forms in the domain.

The distances tested are $z/D = [7.32, 23.5]$, the former corresponding to a supersonic

M_e	Re_e	P_∞	η_e	T_0	T_e/T_∞	D_e	z/D_e
1	1.3×10^6	101325Pa	3.57	299.88K	0.85	13.26mm	[7.32,23.5]

Table 4.3: Computational parameters in case of free jet.

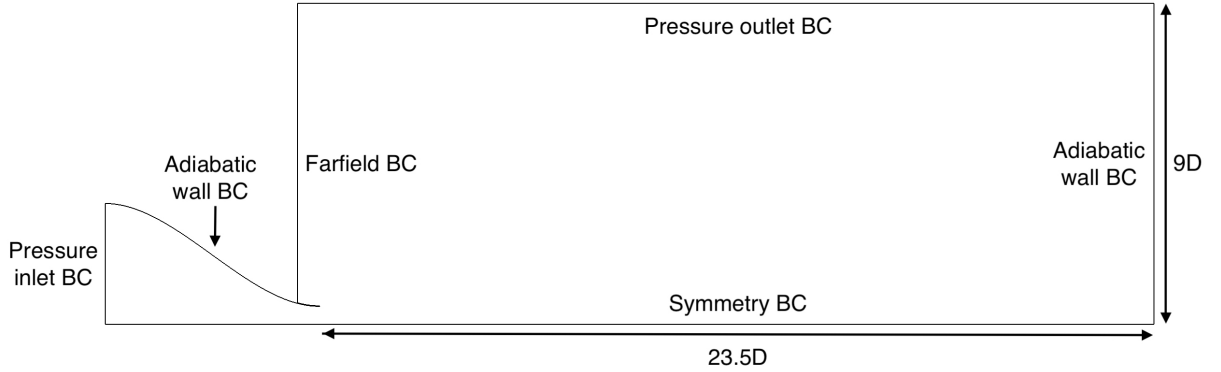


Figure 4.10: Computational domain and boundary conditions used to validate the impinging flow case.

impingement, the latter to a fully developed subsonic one. The subsonic impingement case has also been tested by Chin. et. al. (*NR*), which will provide a numerical reference even in this case.

A convergent nozzle with an outer diameter of $D = 13.26$ mm exhausting to atmospheric pressure P_∞ is employed in this phase of the validation. The throat is sonic and its Reynolds number based on the outlet conditions is estimated similarly as discussed for the precedent case (calorically perfect gas and Sutherland's law) and results to be $Re \simeq 1.3 \times 10^6$. The contour of the device is here replicated by using a spline function. The computational parameters are summarised in Table 4.3 and are once again decided in order to permit a comparison with *NR* in case of $z/D = 23.5$.

In Figure 4.10 the computational domain in case of $z/D = 23.5$ is illustrated together with the boundary conditions (BC), which in this case are specified as follows:

- $P_0 = 687407.3Pa$, $T_0 = 299.88K$ and $u = (1, 0, 0)$ m/s for inlet of the nozzle;
- $P_\infty = 101325Pa$ on the pressure outlet;
- $P_\infty = 101325Pa$, $T_\infty = 288.15K$ and $Ma_\infty = 0.01$ on the farfield;
- no-slip boundary condition on the adiabatic walls.

The symmetry boundary condition is instead imposed similarly to previously done. Finally, both the SA and SST turbulence models have been anew tested and their results

will be discussed in the next section.

4.2.2. Grid independence analysis

Before moving to further analysis is necessary to assess if the chosen grid spacing in section 4.1.2 is suitable also in case of impinging jet. This has been accomplished by considering the same test set-up as previously described for the free-flow case (TM) and arbitrarily placing a wall at a distance of $z/D = 6$. By comparing the numerical results in the region of the stand-off shock, the final mesh refinement will be decided.

In this case, only the spacing correspondent to *mesh3*, *mesh4* and *mesh5* is tested. Similarly to previously done, the axial Mach number evolution is reported in Figure 4.11. As expected, its behaviour along the nearfield region shows similar results as the previous case, where the patterns predicted almost completely match each other. Must be noted that this time the Mach number peak is predicted to be slightly lower than the previous case, which may be related to the numerical uncertainty above described regarding the decrease in pressure across the outlet of the domain.

On the other hand, *mesh3* again poorly predict the discontinuity in the region of the stand-off shock, while *mesh4* and *mesh5* show very similar results.

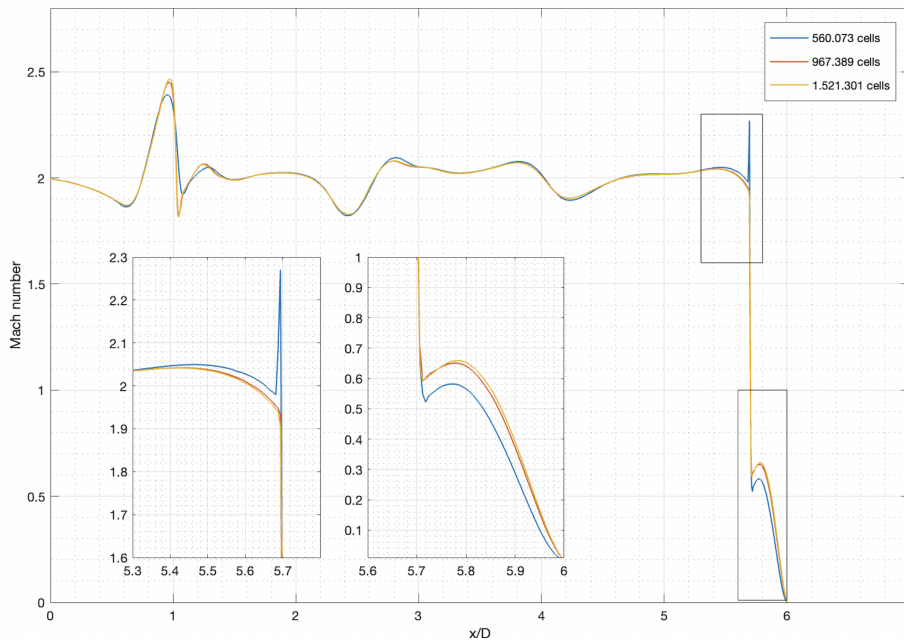


Figure 4.11: Axial Mach number per different mesh refinements - Impinging flow case.

Therefore, *mesh4* represent the best trade-off in terms of accuracy of the simulation and run-time needed to reach convergence. The spacing of *mesh4* will hence be used for all

the simulations described further on by appropriately scaling its value.

In the specific, the computational grid used in the following investigation is composed as the previous case with an additional refinement box placed above the flat plate. The value of the spacing h_{DS} is set according to the following scaling relation:

$$h_{DS} = h_{TM} \frac{D_{e,DS}}{D_{t,TM}}, \quad (4.2)$$

where $D_{e,DS}$ is the outer diameter corresponding to DS, $D_{t,TM}$ the throat diameter of TM and h_{TM} the spacing of *mesh4* obtained from the grid independence analysis. This is made in order to ensure that the grid refinement is preserved when the sizes of the nozzle and of the domain are changed. In this case, $h_{DS} = 1.1E - 04$ and the corresponding mesh is reported in Figure 4.12, being this one the case where $z/D = 23.5$.

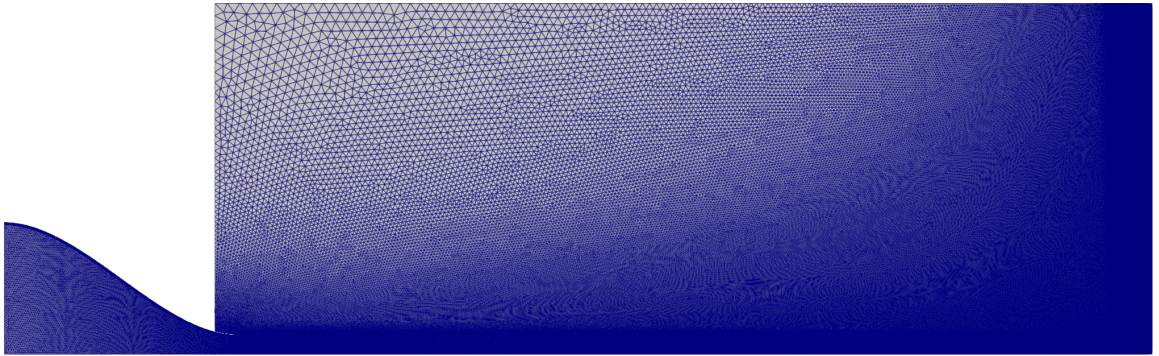


Figure 4.12: Computational grid used to validate the impinging flow case.

4.2.3. Results

The supersonic impingement ($z/D = 7.3$) is firstly examined. The results of the computation are hereafter reported in case of SA turbulence model, since the SST model showed non-reliable predictions in reproducing a highly underexpanded jet, as will be discussed afterwards.

First of all, the conditions corresponding to the nozzle outlet are inspected. As shown in Figure 4.13, the throat is sonic and the outlet-to-ambient pressure ratio is correctly predicted, while the Reynolds number computed with respect the outlet conditions results to be $Re \simeq 1.3 \times 10^6$ and hence matches the experimental data.

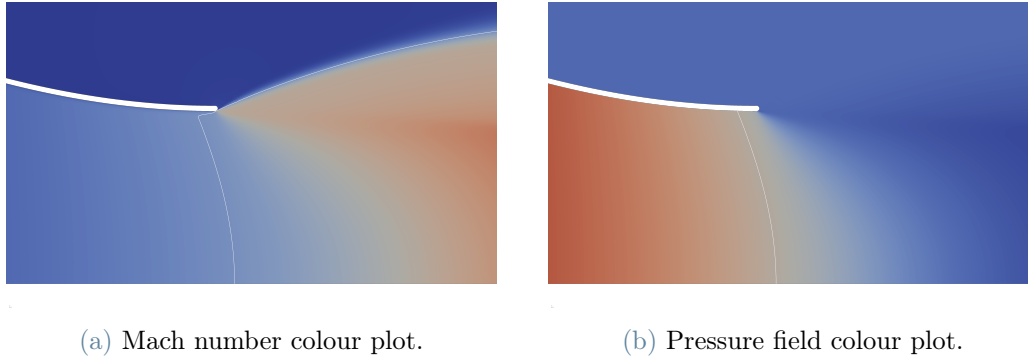


Figure 4.13: Location of the sonic line (a) and the iso-pressure line at $P = 3.57P_\infty$ (b) across the outlet section of the convergent nozzle.

Then, the flow field is described referring to the Mach number colour plot reported in Figure 4.14. As expected, since a highly underexpanded jet is simulated, a Mach disk forms in the domain. Its position is hereby predicted with an accuracy of 97.5% with respect to the reference, being the distance from the nozzle outlet reported in DS $z/D = 1.58$ and the one computed here $z/D \simeq 1.62$. The maximum Mach number is $Ma = 3.53$ and it is reached before the discontinuity. The flow is then re-accelerated to supersonic, forming two additional Mach disk of decreasing strength, before impacting on the flat plate. Finally, the jet is diverted radially outward to form the wall-jet region.

The computed pressure distribution over the plate has been compared with the experimental data of DS and is reported in Figure 4.16. In the graph, the pressure is given as the ratio between the local to stagnation point value, while the radial distance is expressed as nozzle throat radii from the stagnation point. The curves exhibit a central local maxima followed by another off-axis peak, indicating the presence of a stagnation bubble caused by the reversed pressure gradient in the impingement region. The presence of such recirculation region is besides confirmed by the impingement region streamlines pattern shown in Fig. 4.15. This is due to the large total pressure loss introduced by the Mach disk, which is higher with respect the one experienced by the outer region of the flow downstream the oblique shock. Such difference forms at the immediate downstream of the first normal shock and then persists until the flow impinges on the wall.

Comparing the real data with the computed results, can be noticed how the numerical solution correctly predict the formation of the recirculation region above the flat plate. Moreover, the position of the off-axis peak in pressure is, to some extent, correctly positioned. Indeed, in the measurements reported in DS, the maxima is observed at a distance of $r/R_t \simeq 0.6$, while the simulation locates it at $r/R_t = 0.66$. Furthermore, the numerical solution overestimates the pressure for distances approximately beyond the

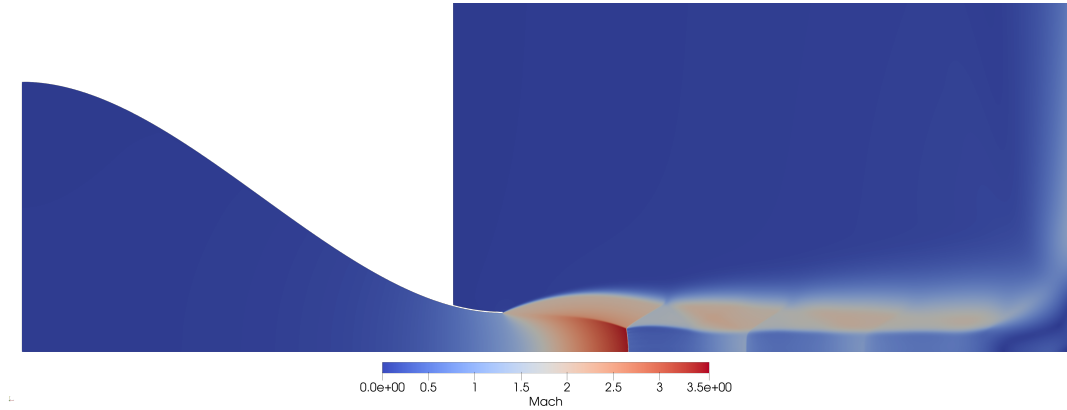


Figure 4.14: Colour plot of the Mach number in case of highly underexpanded jet and impingement distance $z/D = 7.3$.

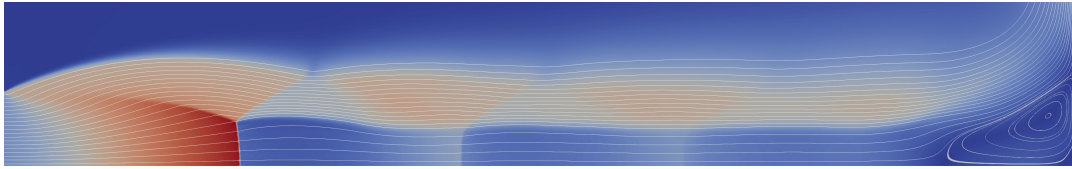


Figure 4.15: Streamlines in case of highly underexpanded jet and impingement distance $z/D = 7.3$.

aforementioned pressure peak. This is again consistent with what observed in the free-jet case regarding the characteristics spreading introduced by the turbulence modeling. However, the overall trend of the pressure distribution reflect the experimental data and hence can be considered reliable for further analysis.

Next, the subsonic impinging case ($z/D = 23.5$) is simulated and the results of this investigation are reported in Figure 4.17. In the graph, the y-axis shows the pressure coefficient, defined as:

$$C_p = \frac{P - P_\infty}{P_0 - P_\infty} \quad (4.3)$$

where P_0 is the pressure in correspondence of the stagnation point. The x-axis instead shows the radial distance from the centre-line scaled with respect the nozzle outlet diameter D_{throat} . The origin in this case corresponds to $y/D_{throat} = 0$. Note that the results obtained with SU2 have been simply mirrored with respect the vertical axis, in order to permit a comparison with all the experimental data.

Accordingly to the previous case, the pressure over the plate is over-predicted in the numerical simulation. At further confirm, the same trend is reported in the NR, although the latter with lower accuracy results. Nevertheless, the computed pressure distribution shows a relative high level of agreement with the experimental data, confirming that the

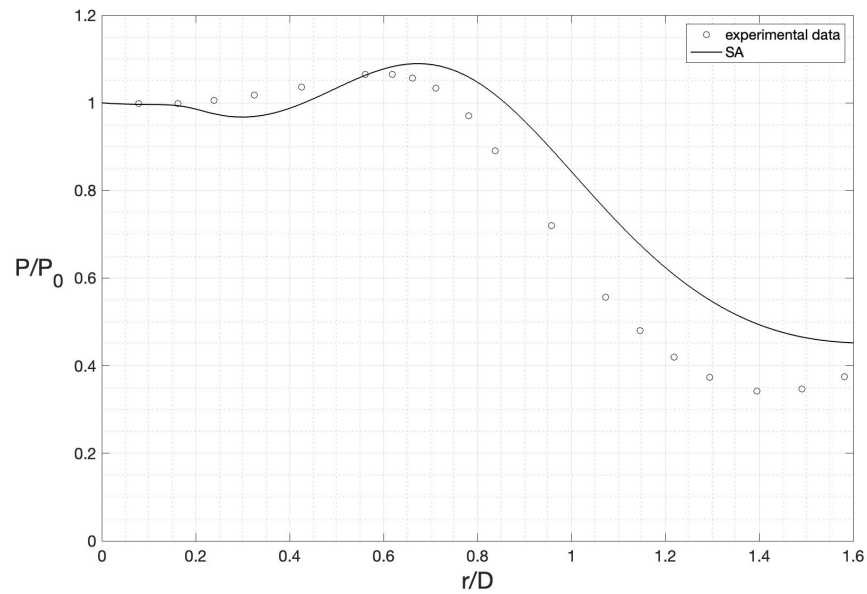


Figure 4.16: Comparison of stagnation region pressure distribution over the plate with the experimental results of Donaldson and Snedeker [10], where the reference pressure P_0 is the centre-line stagnation pressure over the plate.

numerical method is able to predict this kind of jets.

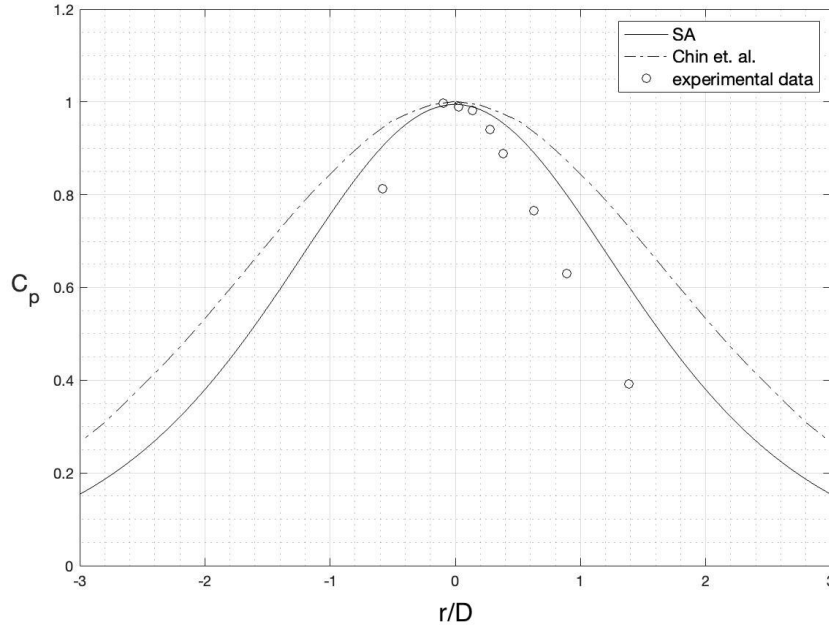


Figure 4.17: Comparison of the pressure coefficient distribution over the flat plate located at $z/D = 23.5$ with the experimental results of Dondaldson and Snedeker [10] and the numerical results of [20].

4.2.4. Numerical uncertainties

As previously mentioned, in case of highly underexpanded jet the SST turbulence model failed in predicting the behavior of the flow field, converging to a wrong solution. Indeed, in the region of the first Mach disk a large overshoot in velocity ($Ma \simeq 5.14$) is numerically predicted to happen in a very confined space, followed by a small recirculation region. A comparison with the results obtained with the SA turbulence model is shown in Figure 4.18, which clearly shows the peak in Mach number. The error then reflects on the rest of the flow field, resulting finally in the absence of the recirculation bubble, which confirms the imprecision of the solution obtained. This may be addressed to a coupling effect between the strong gradient that forms across the discontinuity (i.e. the Mach disks) and the dependence on the gradient itself contained in the formulation of the SST turbulence model, discussed in 3.1.2. Indeed, the turbulence viscosity is subject to a generation across the strong shocks that form in the domain, leading to an erroneous prediction of the turbulence which actively modify the flow field. For clarity, color plots of turbulent viscosity for both turbulence models are shown in Fig. 4.19. As a consequence of the above described error of the SST model, the SA model is preferred in cases where a formation of a Mach disk is expected in the domain. In fact, no turbulent viscosity is

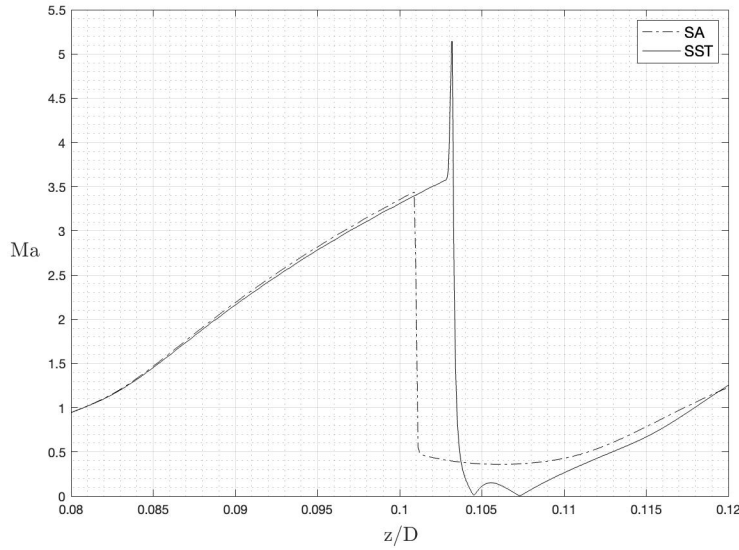


Figure 4.18: Axial Mach number evolution across the Mach disk in cases of SA and SST turbulence model.

generated within the jet core region using the SA turbulence model, while its production is correctly predicted in the shear layer and recirculation region, where viscous effects are expected. Furthermore, similarly to the free-jet simulation, the static pressure across the outlet results lower with respect the imposed boundary value. Anyway, this kind of numerical error takes place at a distance sufficiently high that can be considered not relevant in simulating the impinging region.

4.3. Conclusions

In conclusion, the axi-symmetric solver of SU2 shows overall good quality in simulating a free and impinging underexpanded jet. The analysis conducted in this chapter also showed that the Shear Stress Transport model produces better results whether the flow to be simulated is moderately underexpanded. On the other hand, the Spalart-Allmaras turbulence model apparently is more reliable than the Shear Stress Transport model provided that a formation of a Mach disk is expected in the flow field. Additionally, worth mentioning that both the models considerably overestimate the decay of the characteristics of the jet at high distances from the nozzle exit section. Nevertheless, the final study contained in this work will focus on nozzle-to-plate distances smaller than $z/D = 6$ and hence this issue will not be considered relevant. Finally, since in the ensuing investigation we also want to inspect the impact of a Mach disk on the ground effect, henceforward only the Spalart-Allmaras turbulence model will be considered.

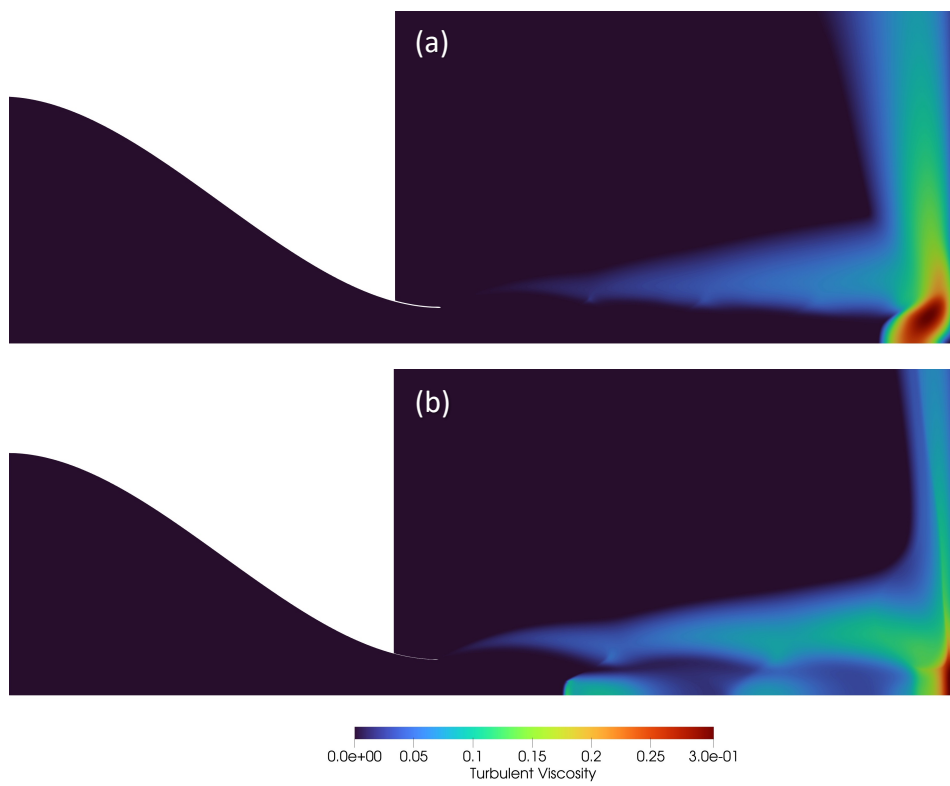


Figure 4.19: Colour plots of the turbulent viscosity in case of SA (a) and SST (b) turbulence models in case of $z/D = 7.3$.

5 | Tests and Results

In this last chapter, the final investigation performed is reported. Aim of this analysis is to investigate how far the shape of the nozzle has an impact on the flow field generated by an underexpanded jet impingement. To accomplish this goal, three different nozzles have been considered and the flow field generated has been analysed firstly in free jet configuration, then in ground effect. Furthermore, to cover a wider range of cases, the exit-to-ambient pressure ratio and the nozzle-plate distance are also varied.

The simulation set-up is chosen accordingly to what employed in Chapter 4, in order to obtain results that can be considered reliable within a certain range of validity.

In the first section of this chapter the test cases are introduced. Then, the simulations outcomes are presented for the free-jet and finally for the impinging-jet, together with the discussion of the results.

5.1. Test Cases

In order to investigate the impact of the nozzle geometry in ground effect, different axisymmetric convergent-divergent nozzle have been taken into account. The shape of the divergent section is chosen accordingly to previous computations performed at the André Jaumotte Laboratory of the Université Libre de Bruxelles, where different nozzles have been designed and will be tested in the future. In this manner, this work proposes to predict, to a certain extent, the flow field features that should be observed in future experimental tests and especially whether significant differences in the flow field generated by different nozzle shapes are expected or not.

The nozzle size is defined by the plant capability in terms of delivered mass flow, resulting in a throat diameter of $D_t = 1$ mm. The design Mach number at the nozzle outlet is $Ma = 1.7$ and the corresponding area ratio is $A_e/A^* = 1.338$, based on the NACA tables for compressible flows. The nozzles are fed with pressurised N_2 and exhaust in a quiescent environment at ambient pressure. It should be noted at this point that the flow configuration presented hereafter is unheated, which can be considered as a simplified version of real systems.

In this work the nozzles tested are three and differ only for the shape of the divergent section. The convergent part has an inlet diameter of $D_i = 2mm$ and a length of $L_{conv} = 2mm$ and it is coincident for all the nozzles. The contour of this section has been replicated by means of a spline function, as already done previously. Regarding the divergent section, the first nozzle ($N1$) has a contoured profile and is designed with the theory of characteristics. Both the second ($N2$) and the third ($N3$) have instead a conical shape, with different length. In particular, $N2$ is $15mm$ long and has a semi-diffusive angle of $\varepsilon_2 \simeq 3^\circ$, while $N3$ is $25mm$ long with $\varepsilon_3 \simeq 2^\circ$. In this manner, the value of the semi-diffusive angle spans from $\varepsilon_2 \simeq 0^\circ$ to $\varepsilon_2 \simeq 3^\circ$ and its impact on the flow field will be discussed afterwards.

The profile of the nozzles are illustrated in Figure 5.1, where only half of the contours is visible, being the nozzles axisymmetric. Their total length is also reported.

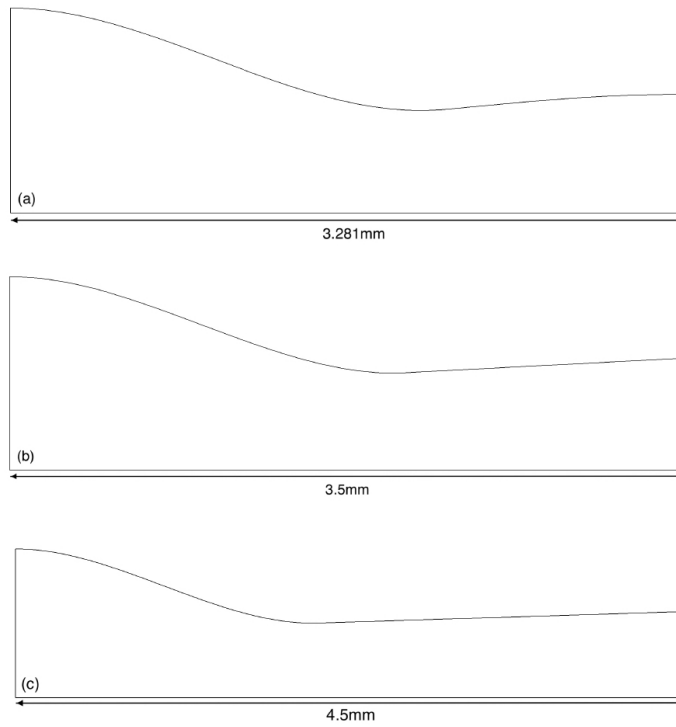


Figure 5.1: Illustration of half a section of the nozzles with their total length, where: (a) $N1$; (b) $N2$; (c) $N3$.

The nozzles are tested both in free-jet and impinging-jet configurations. To cover a wider range of cases, the nozzle pressure ratios chosen are $\eta_0 = [6.9, 12.4]$, which, given the expansion ratio, correspond to exit-to-ambient pressure ratio of $\eta_e = [1.4, 2.5]$ (respectively indicated hereafter as $NPR1$ and $NPR2$). In this manner, the purpose is to simulate the impingement of both moderately and highly underexpanded jet.

M_e	Re_e	P_∞	η_0	η_e	T_0	$(z/D)_w$
1.7	1.2×10^5	101325Pa	[6.9,12.4]	[1.4,2.5]	288K	[1.8,2.5,3.5]

Table 5.1: Computational parameters used in all the computations.

In case of impinging jet, the nozzle-to-plate distances tested are $(z/D)_w = [1.8, 2.5, 3.5]$ and are henceforward indicated as D1, D2 and D3, in order. The former distance is chosen such that the regular reflection of the intercepting shock on the axis in case of moderately underexpanded jet would be anticipated by the presence of the wall, whereas the latter such that the distance is large enough to allow the formation of a fully developed shock cell in case of highly underexpanded jet. The distance D2 represent a midway configuration between the other two cases. The parameters used for all the computations are summarised in Table 5.1.

The computational domain is, likewise the validation analysis, composed by the nozzle and external field. The latter stretches from the nozzle exit section in both radial and axial directions. For the free-jet configuration, the height of the computational field is set to be $r/D = 3.25$, while the distance of the outlet domain from the nozzle exit plane is in all the instances chosen such that the out-going flow is subsonic, in order to avoid instabilities due to supersonic flow boundary condition ¹. Instead, for the impinging jet case the axial length of the computational domain is imposed by the chosen wall distance, while its height in radial direction according to the just described criterion (subsonic outlet), as in this case the upper boundary corresponds to the domain outlet section.

The mesh spacing is computed similarly to Eq. 4.2 and results to be $h = 8.4E - 6$. As an example, the mesh used in case of N1 and D3 is illustrated in Figure 5.2, together with the boundary condition employed, where in particular:

- $P_0 = [700000, 1250308.5]Pa$, $T_0 = 288K$ and $u = (1, 0, 0)$ m/s at the nozzle inlet;
- no-slip condition for the adiabatic walls with no heat-flux;
- asymptotic conditions and $Ma_\infty = 0.01$ for the farfield BC;
- $P_\infty = 101325Pa$ for the upper boundary of the domain.

¹As a matter of fact, a supersonic outlet boundary condition has been firstly tested but it led to divergence, probably due to co-existence of supersonic and subsonic flow across the domain outlet.

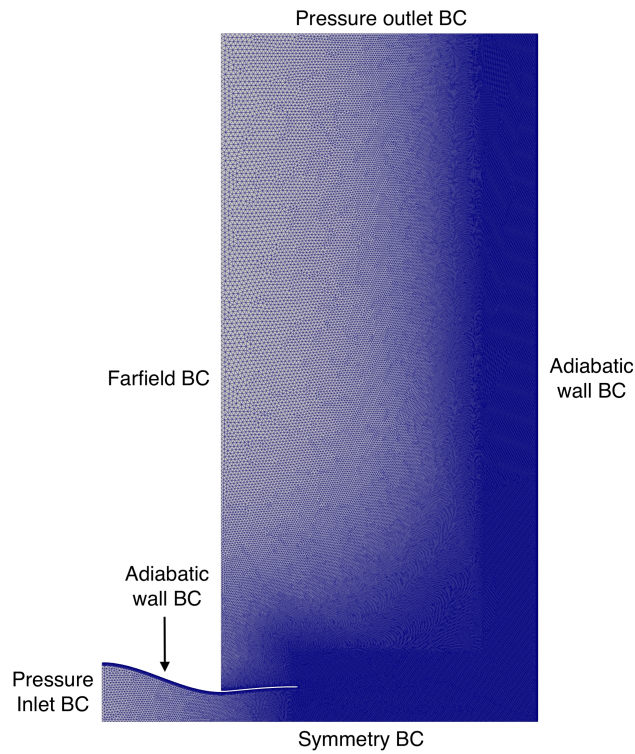


Figure 5.2: Computational grid and boundary conditions employed in case of contoured nozzle and distance $D3$.

Furthermore, from now on the all the quantities are reported in non-dimensional form, which are defined as follow:

- The axial (z) and radial (r) coordinates are made dimensionless with respect the nozzle outer diameter D ;
- The velocity is expressed in terms of Mach number;
- The pressure is reported as static-to-total ratio P/P_0 , where the reference pressure P_0 corresponds to the reservoir condition.

All the simulations are initially performed in an open boundary configuration in order to evaluate the differences in the free jet structure. Successively, similar analysis is carried out in case of impacting jet, where the axial and radial evolution of the flow field will be investigated, together with the estimation of the pressure distribution over the plate.

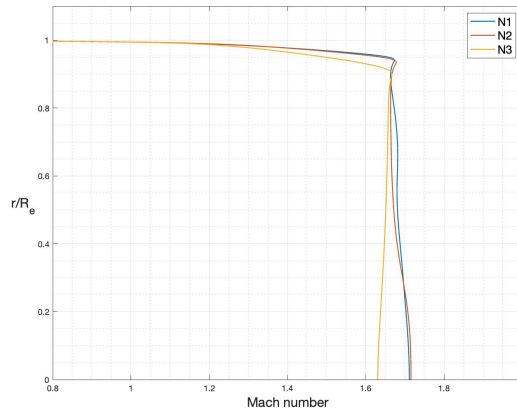


Figure 5.3: Comparison between the exit mach number profile corresponding to three different nozzle shapes.

5.2. Results

5.2.1. Free flow configuration

To assess the impact of the nozzle geometry on the flow field, its homogeneity across the nozzle exit sections is firstly investigated. In Figure 5.3 the exit Mach number profiles corresponding to the three nozzles are illustrated, where on y-axis is reported the ratio between the radial coordinate and the outer radius R_e and $r/R_e = 0$ refers to the centreline. The profiles appear to be homogeneous across the whole outlet with exception of the region where a boundary layer forms. From the graph, the effect of the length of the nozzle can be also evaluated. Indeed, N1 and N2 have similar length and the curves almost overlap, while some differences can be observed regarding N3. In particular, the average outlet Mach number is in this case lower than the design value by 3% circa. This is due to blockage effect introduced by the thickness of the boundary layer, which radial extension grows with longer divergence section, reducing then the effective discharge area and in turn the exit Mach number. The flow uniformity across the outlet and the slight difference in exit Mach number finally suggest that the main impact on the internal flow field development is not the actual shape of the nozzle but rather the length and thickness of the boundary layer.

Next, the sensitivity of the external evolution to the used device is investigated, first regarding a moderately underexpanded jet (NPR1) and then for a highly underexpanded jet (NPR2).

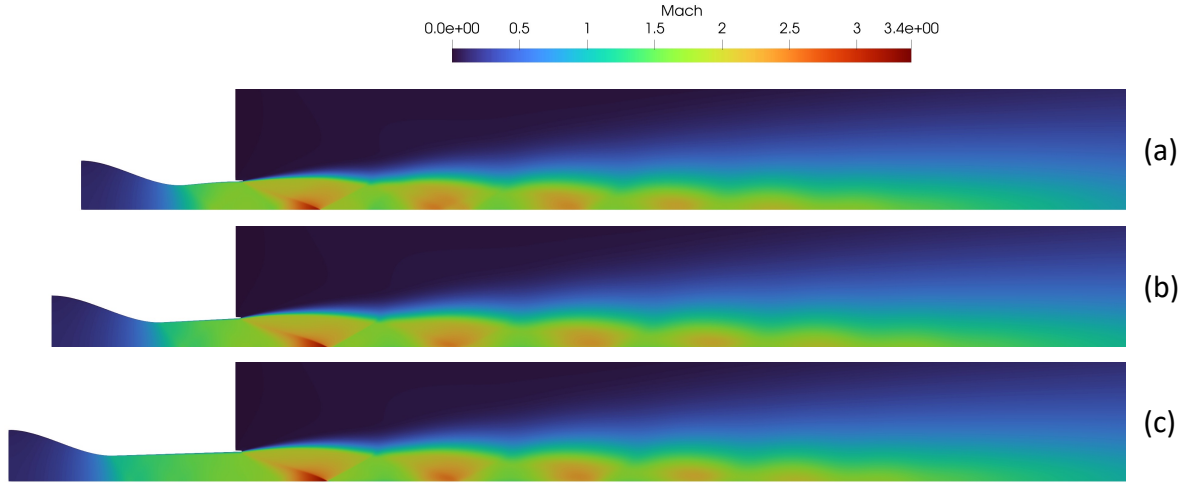


Figure 5.4: Color plot of the Mach number of a moderately underexpanded jet NPR1 in cases of (a) N1; (b) N2; (c) N3.

Moderately underexpanded impinging jet:

In case of NPR1, the Mach number colour plots of the three nozzles are represented in Figure 5.4. As can be seen, the overall flow structure does not present any significant difference at a first sight and resembles the moderately underexpanded jet. Small differences within the order of 3.5% are predicted in the location of the first intercepting shock and similarly the length of supersonic core appears not significantly sensitive to the geometry of the nozzle, being $z/D \simeq 14.9$ irrespective the used device. However, even in this case the velocity decay due to turbulence modeling must be taken into account and therefore the effective length of the supersonic region would be larger in a real-case scenario.

On the other hand, the development of the nearfield zone shows some relevant differences, as in first place can be deduced by the axial Mach number evolution illustrated in Figure 5.5. As expected, the maximum velocity is reached upstream the first intercepting shock and is slightly higher in case of N2 and N3, being $Ma_{N2} = 3.4$ and $Ma_{N3} = 3.3$, while in case of contoured nozzle it results to be $Ma_{N1} = 3.1$. The intensity of such shock is instead rather different and increases with the divergence angle ε , being lower in case of N1 and the highest for N2. Specifically, the predicted shock is oblique in cases of N1 and N3 and turns to a normal one with the nozzle N2, as suggests the subsonic speed reached downstream such shock. This indicates that a formation of a Mach disk is already predicted at low exit-to-ambient pressure ratio whether the divergence angle is sufficiently high. This could lead one to hypothesise that the local inclination of the streamlines is higher in case of nozzle N2 ($\varepsilon_2 = 3^\circ$), hence requiring a stronger compression to re-align

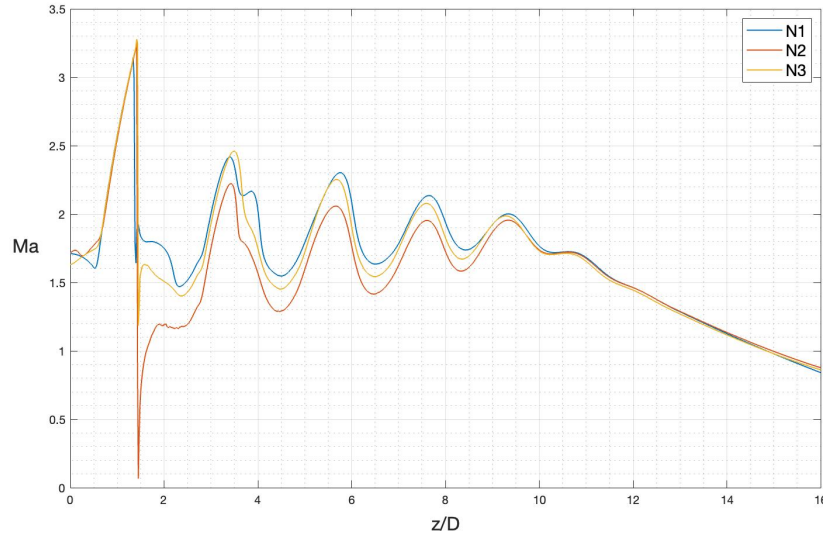


Figure 5.5: Axial Mach number evolution in case of NPR1 for different nozzle geometry.

the flow with the axis.

Additionally, must be noticed that the very low velocity reached downstream the shock in case N2 may represent a numerical error, as although the expected velocity is subsonic, the predicted value is rather low. In fact, the value numerically simulated is lower compared to the one theoretically predicted by the relations for quasi-one-dimensional flow across normal shock waves ($Ma = 0.45$). This may be attributable to possible local lack of accuracy of the employed grid, that may not be enough to catch the strong gradients which are expected to form in correspondence of the axis. Nevertheless, can be considered that the issue has a local effect, as the successive flow evolution is similar to the other cases.

The losses introduced by such shock are then reflected on the successive flow field evolution, as the velocity is lower corresponding to higher shock intensity, although the overall trend is similar. Contrarily, the farfield behavior ($z/D > 10$) results to be coincident for all the cases.

In Figure 5.6 the radial profile of the Mach number are then represented for four distances, together with an illustration of the corresponding axial location of the plots, which in this case are $z/D = [1, 2, 4, 6]$. Coherently with the axial Mach number curves, the graphs confirm the different evolution of the core region, where the flow velocity in case of N1 is always higher than the other two cases due to the losses introduced by the intercepting shock, except for distance $z/R = 1$ which is located upstream the same shock. The jumps in Mach number that can be observed in cases $z/D = 1$ and $z/D = 2$ are consequence of the different stages of flow expansion due to the oblique shocks. Must also be noticed

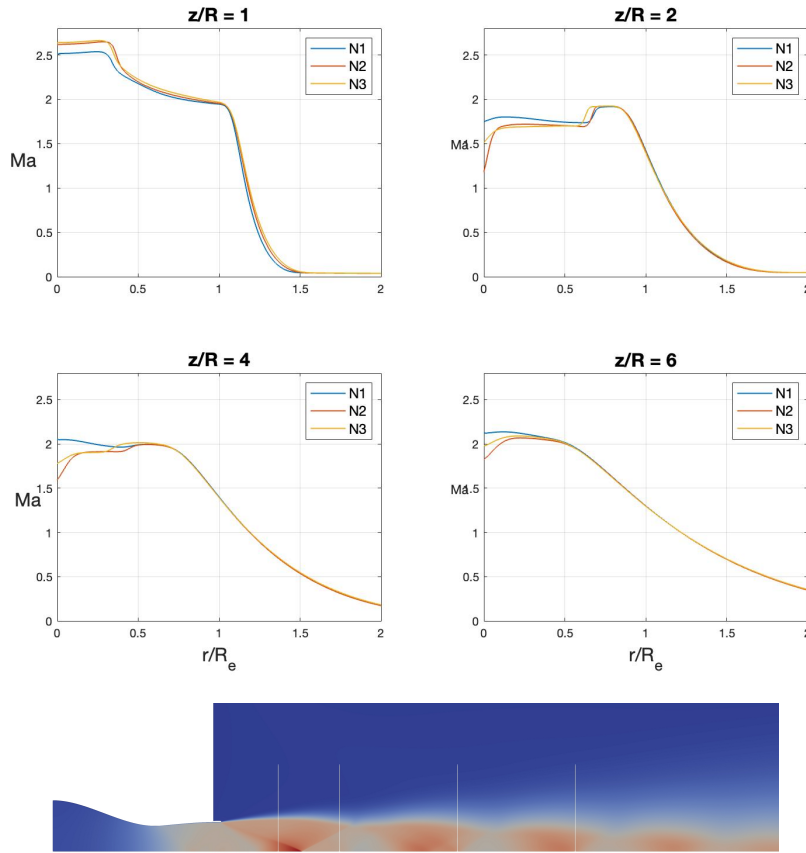


Figure 5.6: Comparison of the streamwise Mach number profiles in the radial direction for different nozzle geometries at different axial locations in case of NPR1. In the graph R_e refers to the radius of the outlet section. On the bottom, a visualization of the location of the radial lines.

that the behavior of the curves in correspondence of the axis ($r/R_e = 0$) represents a numerical uncertainty, as the flow is expected to be perfectly symmetrical with respect the centre-line and hence the local inclination of the curves should be zero. This may be once again attributable to a lack of grid resolution in both radial and axial directions in correspondence of the axis, where rapidly varying gradients are expected and may be not properly captured by the employed grid.

On the other hand, the flow discontinuities progressively smooth down moving radially outward. Then, all the curves finally merge, indicating that the shear layer is not significantly influenced by the geometry of the nozzle.

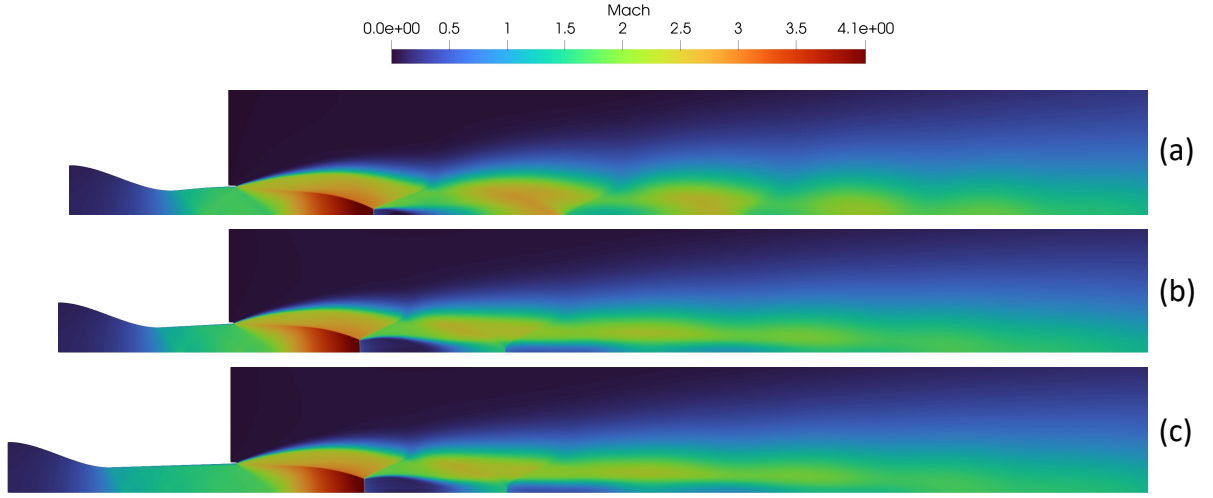


Figure 5.7: Color plot of the Mach number of a highly underexpanded jet NPR2 in cases of (a) N1; (b) N2; (c) N3.

Highly underexpanded impinging jet:

The same analysis has been carried out regarding the highly underexpanded jet (NPR2) and it is discussed in the following. Before commenting the results is however here anticipated that, although the simulation concerning N1 has completely reached convergence (-11 residual in density), the same cannot be said for N2 and N3. Indeed, the order of magnitude of the residuals in density is, despite low, limited to values of $rms_\rho = -7$ and $rms_\rho = -8$, respectively. Specifically referring to the centre-line only, some oscillations in residual are detected at distances higher than $z/D = 11.2$ in both the cases, while upstream the same value the residual value is restricted to $rms_\rho < -10$. Nevertheless, since in this work we are focusing on the nearfield region, the results obtained can be in any case discussed to some extent and will be hence commented in the following analysis.

As the previous case, in Figure 5.7 the color plots of the Mach number are illustrated. The jet resembles the highly underexpanded jet in all the cases, as suggested from the formation of a Mach disk downstream the nozzle exit. The diameter of the such disk changes with the nozzle geometry, being $D_{disk} = 0.117D$ for the contoured nozzle, $D_{disk} = 0.188D$ for the conical N2 and $D_{disk} = 0.235D$ for the conical N3. Its axial location is similarly computed in case of conical nozzles and results $(z/D)_{disk} = 2.2$ (within a difference of 2%), while it is $(z/D)_{disk} = 2.35$ for the contoured N1. Additionally, the intensity of the shock is the highest for nozzle N1 (highest velocity reached before the disk).

Moreover, as visible in the figure, the formation of an additional shock disk is predicted in cases of N2 and N3. Its formation then reflects on the following flow structure, as confirmed by the axial Mach number evolution reported in Figure 5.8, which is similar for the conical nozzles and very different for the contoured one. In particular, it must be noticed that the

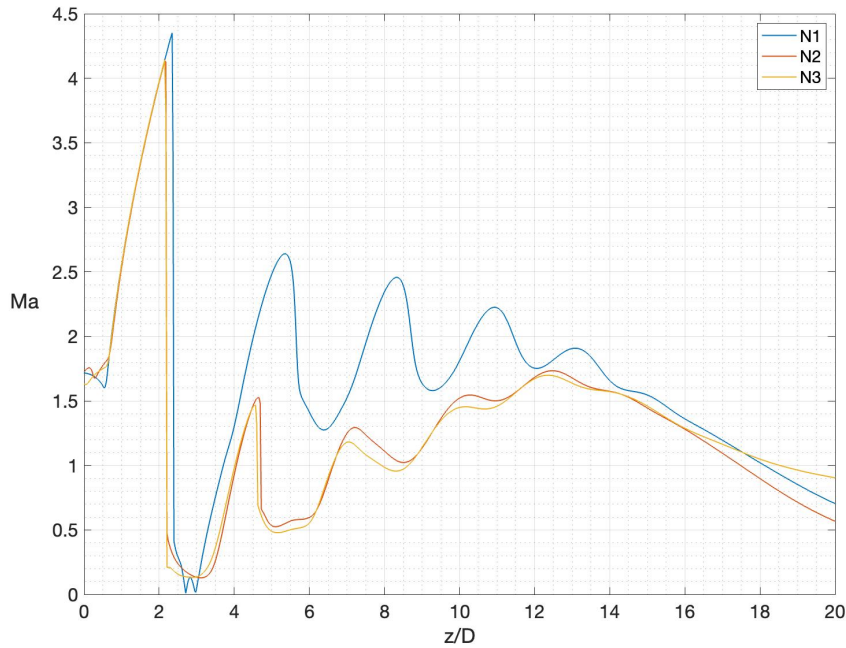


Figure 5.8: Axial Mach number evolution in case of NPR2 for different nozzle geometry.

Mach number value just downstream the shock is coherent with the standard relations for normal shock for N1 and N2, while it is slightly lower for nozzle N3. Nevertheless, the presence of stagnation points is detected along the axis in case of N1, which represents a numerical error probably related to the grid refinement along the axis, as although the flow is locally decelerated to subsonic velocity, regions at zero velocity are unlikely to be formed in the flow field. Additionally, one may address the problem to the intrinsically unstable nature of the highly underexpanded jets, which is not represented by the steady state simplification employed in this work.

Successively, the flow evolves as a moderately underexpanded jet in case of nozzle N1, where the oscillations are attributable to the diamond structures which form. Indeed, the Mach number persists above the sonic value until the core region is completely dissipated. On the other side, in cases of conical nozzles the presence of an additional Mach disk has the effect of reducing the speed to subsonic values a second time, although the intensity of the second shock is evidently lower. The potential core is then re-energised by the outer region diffusing into the inner part, until the usual decay in the farfield is predicted.

The radial profiles of the Mach number are next reported in Figure 5.9, where the axial locations are chosen to be coincident as previously done for NPR1. Similarly to the moderately underexpanded case, the simulations predict different behaviors of the core region, except for small axial distances from the nozzle outlet plane ($z/R = 1$), where

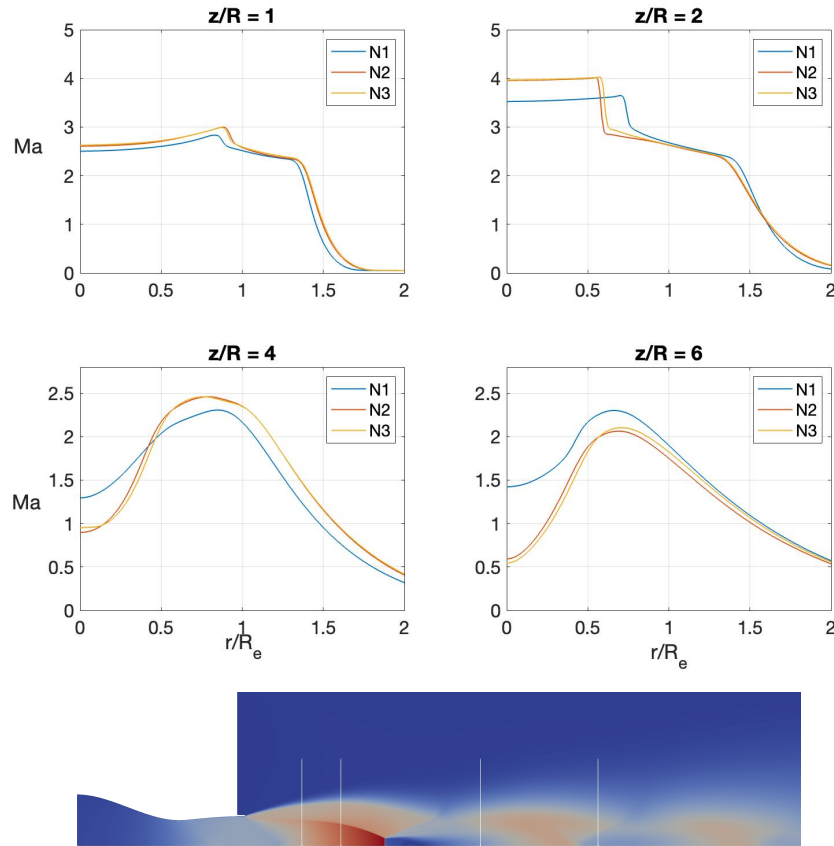


Figure 5.9: Comparison of the streamwise Mach number profiles in the radial direction per different nozzle geometry at different axial locations in case of NPR2. In the graph R_e refers to the radius of the outlet section. On the bottom, a visualization of the location of the radial lines.

instead the profiles almost overlap. Once again, at higher radial coordinates the curves behave similarly, confirming that the shear layer is not significantly influenced by the nozzle geometry. As a conclusion, one can say that the most relevant differences that have been acknowledged in a free flow structures regard the intensity of the oblique and normal shocks that form in the domain, which then reflects on the rest of the flow field. In the radial direction, is instead found that the behavior of the shear layer is not consistently sensible to the kind of nozzle used.

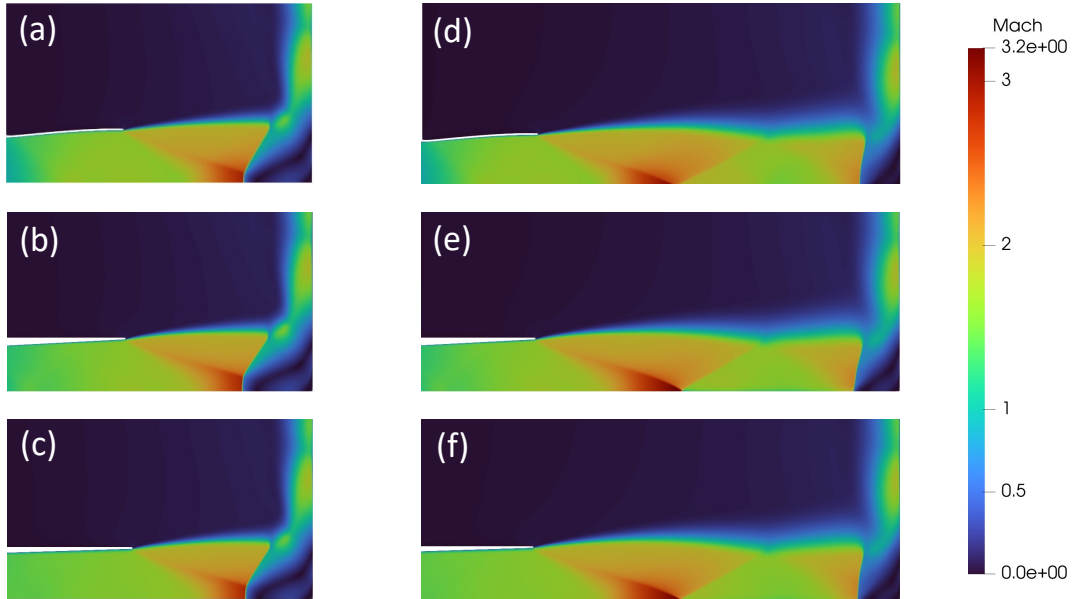


Figure 5.10: Mach number colour plots of an impinging moderately underexpanded jet in cases of (a) N1, (b) N2, (c) N3 and D1 on the left; (d) N1, (e) N2, (f) N3 and D3 on the right.

5.2.2. Impinging flow

Finally, in this section the results for the impinging jet configuration are reported. This goal is accomplished considering the axial and radial evolution of the flow, evaluating the pressure distributions over the flat plate and at last assessing if there are some differences in the behavior of the radial wall-jet.

Moderately underexpanded impinging jet:

As seen for the free-jet case, the results are firstly discussed for the moderately underexpanded jet (NPR1). In Figure 5.10, the representations of the Mach number colour plots are reported for all the nozzles and for the distances D1 and D3, where in particular it is magnified the impingement region. The flow field of the nozzle-to-plate spacing D2 appears similar to the case D3 and hence is not here reported.

As illustrated, the numerical method is able to correctly capture all the expected flow field features, as the presence of a discontinuity in front of the flat plate and the ensuing formation of a wall-jet region. Moreover, some relevant flow field differences can be acknowledged between D1 and the other two cases considered in this work.

In particular, for D1 a Mach disk forms in the domain instead of the regular reflection

of the intercepting shock displayed for the free-jet. This is due to the proximity of the wall, where the formation of the lambda structure prevent the formation of the plate shock. Such behavior of the moderately underexpanded jets also finds correspondence in literature [33], as described in 2.4.

On the other hand, at larger wall distances (both D2 and D3), the intercepting shock reflects regularly on the axis. As a result, the flow downstream the reflection point persists supersonic. In this case, the impingement results in the formation of a normal shock - the plate shock - in front of the wall (see Figure 5.10, distance D3).

Nevertheless, the impingement region is characterized by the generation of a stagnation bubble regardless of wall distance and nozzle considered. The stagnation bubble is better detailed in the following.

The flow thence undergoes in all the cases a strong compression to subsonic velocity and is finally diverted radially outward, where expands again to supersonic velocity in the wall-jet region.

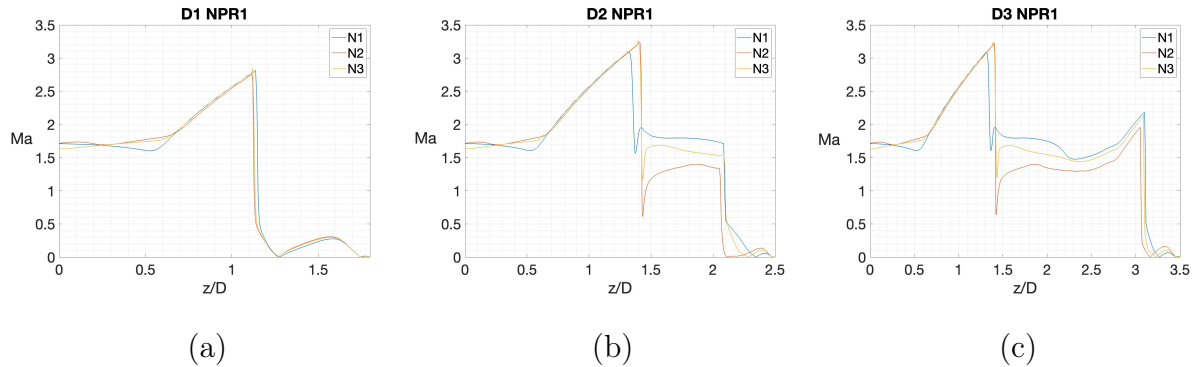


Figure 5.11: Mach number axial evolution in case NPR1 impinging jet on a flat plate per different nozzle geometries.

Figure 5.11 reports the comparison in Mach number axial evolution between the three nozzles considered and at varying nozzle-to-wall distance. In the graphs, the origin refers to the nozzle exit plane, while the highest abscissa corresponds to the position of the wall. Once again, it can be noticed that in case of distance D1 (a) the wall is placed sufficiently close to the nozzle outlet to prevent the reflection of the intercepting shock on the axis. The unique discontinuity observable is indeed attributable to the Mach disk, which is immediately followed by a stagnation point.

The stand-off distance δ , defined for D1 as the distance of the Mach disk from the wall in axial direction, results $\delta \simeq 0.66D$ within a difference of 3% between the three nozzles for distance D1. Then, downstream the Mach disk and the stagnation point, the following

rise in Mach number represents a region of flow reversal which, as said before, suggests the presence of a flow reversal area, i.e. the recirculation bubble.

Furthermore, as the intercepting shock reflection on the axis is anticipated by the Mach disk, the differences in flow field between the three nozzles appear rather small, coherently with the results obtained in case of free jet (see Figure 5.11 (a)), which showed that the differences are generated when the first shock cell is fully developed.

On the other hand, in cases of distances D2 and D3 the intercepting shock reaches the axis where it is reflected (cases (b) and (c) in Figure 5.11). Likewise the free-jet case, the intensity of such shock is sensible to the nozzle shape and the following losses have consequences on the downstream flow evolution. Once again, the presence of a small Mach disk is detected for the nozzle N2, as the flow results locally subsonic downstream the intercepting shock reflection.

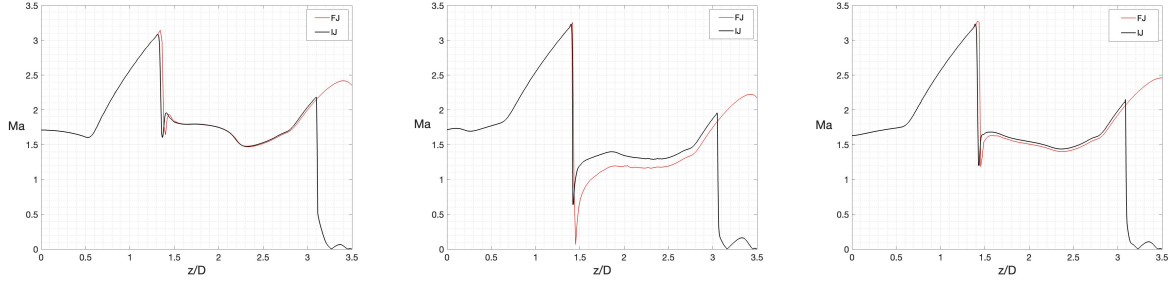
Furthermore, the velocity of the flow impacting the wall decreases with higher nozzle diffusive angle ε , from N1 to N3 and finally N2. Consequently, the plate shock is comprehensibly weaker at lower velocity. The stand-off distance δ (defined now as the distance of the plate shock from the wall) is then different depending on the nozzle as reported in Table 5.2, together with the results obtained for the distance D1. Accordingly, the dimension of the recirculation region is bigger at higher values of δ (N2), spanning from the plate shock to the wall coordinate.

	N1	N2	N3
D1	0.65	0.67	0.67
D2	0.40	0.44	0.42
D3	0.39	0.44	0.41

Table 5.2: Stand-off shock distance for different nozzle shapes and different wall distances. The value of δ is non-dimensional with respect the nozzle outer diameter D .

For completeness, a comparison between the axial Mach number in the free and impinging jet cases for the nozzle-to-plate distance D3 is reported in Figure 5.12. Results apparently match correctly between the two configurations for nozzles N1 and N3, while some discrepancies can be noticed for the nozzle N2. In particular, although the flow behavior upstream the intercepting shock is rather coincident and downstream the intercepting shock it is once again computed to be subsonic, the intensity of such shock appears to be different for the two cases. Indeed, it results to be $Ma \simeq 0.6$ for the impinging jet, higher this time with respect the expected value computed with the standard relations for normal shocks ($Ma = 0.45$). However, the overall flow development seems to be similar

in both the cases. Similar results are obtained for the distances D1 and D2. Next, the



(a) Nozzle N1 and D3 case. (b) Nozzle N2 and D3 case. (c) Nozzle N3 and D3 case.

Figure 5.12: Comparison between the NPR1 axial Mach number evolution in cases of free jet (FJ) and impinging jet (IJ) configurations for different nozzle geometries.

pressure pattern generated over the flat plate is discussed. The wall pressure distributions are shown in the plots in Figure 5.15. In this case, the x-axis reports a wall coordinate which is zero at the jet centre-line and grows moving radially outward, while the pressure is made non-dimensional with respect to the reservoir total pressure ($P_0 = 700000 Pa$ for NPR1). in order to provide a further estimation of the pressure loss generated during the external expansion of the flow.

As shown, in all the cases is detected an off-axis peak in pressure, which is the reason for the appearance of the stagnation bubble. Such peak is clearly more pronounced in case of distance D1 (a), due to the high pressure loss generated by the Mach disk in the central region of the jet compare to the outer region where the flow pass through an oblique reflected shock. Such difference persists over the wall, which explains the pressure pattern. For clarity, in Figure 5.13 shows the color plot of the total pressure loss, which is defined as:

$$Y = \frac{P_0 - P_t}{P_0}. \quad (5.1)$$

being P_t the local total pressure and P_0 the reservoir pressure. As illustrated, losses are predicted where viscous effects are expected, i.e. boundary layer and shear layer, as well as in the recirculation region downstream the lambda structure.

On the other hand, when the impingement results in the formation of a plate-shock (D2 (b) and D3 (c)) the total pressure decrease downstream the shock is approximately constant across the whole span of the discontinuity, as testified by the rather contained off-axis peak in pressure. Consequently, the radial width of the recirculation region appear to be more contained, as shown in Figure ??.

Additionally, can be noticed that the decrease in pressure with respect the reservoir value is more pronounced at distance D1, due to the higher velocity reached before the Mach

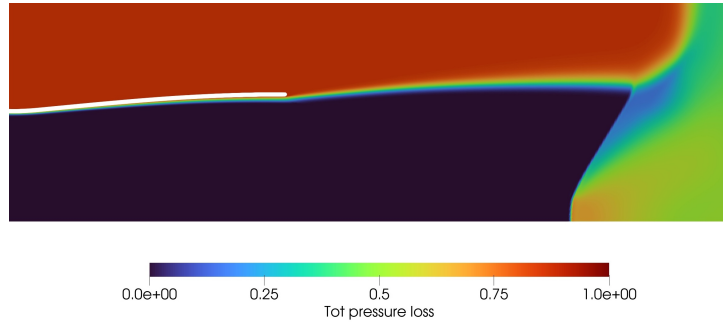


Figure 5.13: Visualization of the total pressure loss across the domain in case of N1, D1 and NPR1.

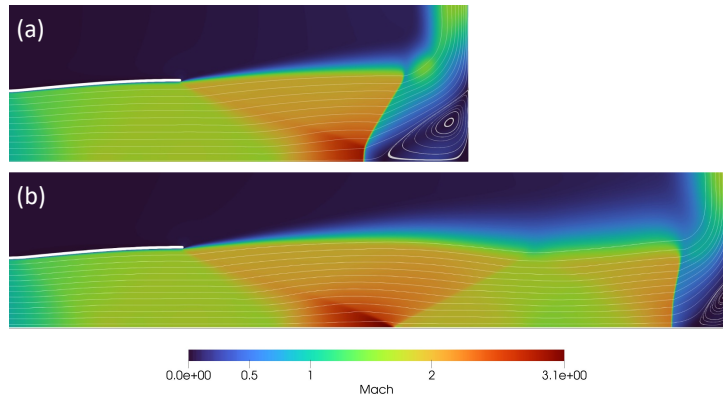


Figure 5.14: Visualization of the streamlines in case NPR1, N1 and D1.

disk ($Ma \simeq 2.8$) and hence higher intensity of the normal shock, while is the lowest in case of D2, when the impingement happens at lower velocities due to the stage of flow compression caused by the reflected shock.

Regarding the geometry of the nozzle influence, one can say that it has a mild effect on the pressure distributions, as the differences are rather contained especially whether the wall is placed at short distance (D1). Once again, at high nozzle-to-plate spacing the losses are the lowest in case of N1 and the highest in case of N2, due to the intensity of the intercepting shock discussed previously.

Finally, all the curves merge and have coincident behavior once they overcome the pressure peak, where the wall-jet is said to begin. The successive oscillations in pressure are due to the local acceleration and deceleration which the flow undergoes in the wall-jet regime.

Highly underexpanded impinging jet:

The above investigation has been alike performed in case of highly underexpanded jet (NPR2) and is next detailed. The Mach number colour plots are illustrated in Figure 5.16 and correspond to the distances D1 and D3. The flow visualization for the distance

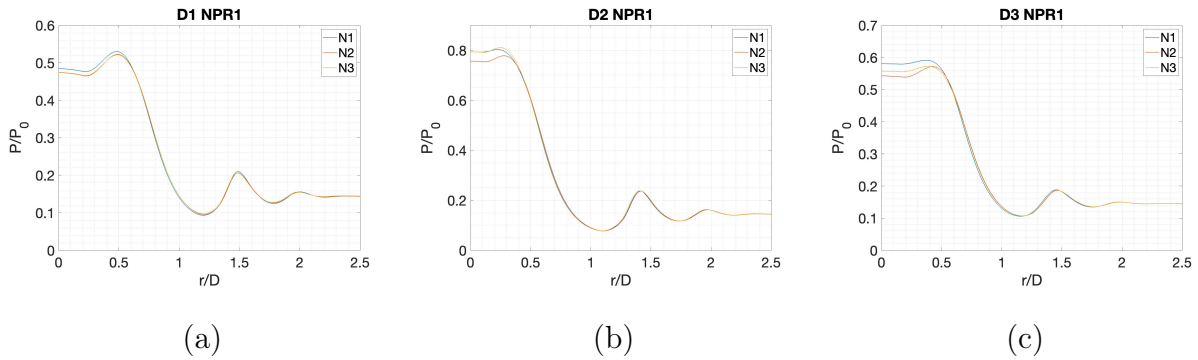


Figure 5.15: P/P_0 distributions over the flat plate in case of moderately underexpanded jet NPR1 per different nozzle geometries and distances. In the graphs, P_0 refers to the reservoir condition.

D2 resembles the case D1 and hence is not here reported.

As a matter of fact, the results obtained in this phase regarding the distance D3 correspond to rather low order of convergence ($rms_\rho = -6$), as the numerical computations resulted stiff to converge. In fact, high residual persists across the Mach disks that form in the domain. A possible solution for this issue may be to make use of an unsteady simulation, as the flow field is expected to be strongly unsteady. Nevertheless, the obtained flow field appear to be physically plausible and hence the results are anyway discussed, despite being less reliable. On the other hand, the simulations in cases of D1 and D2 completely converged and are next discussed.

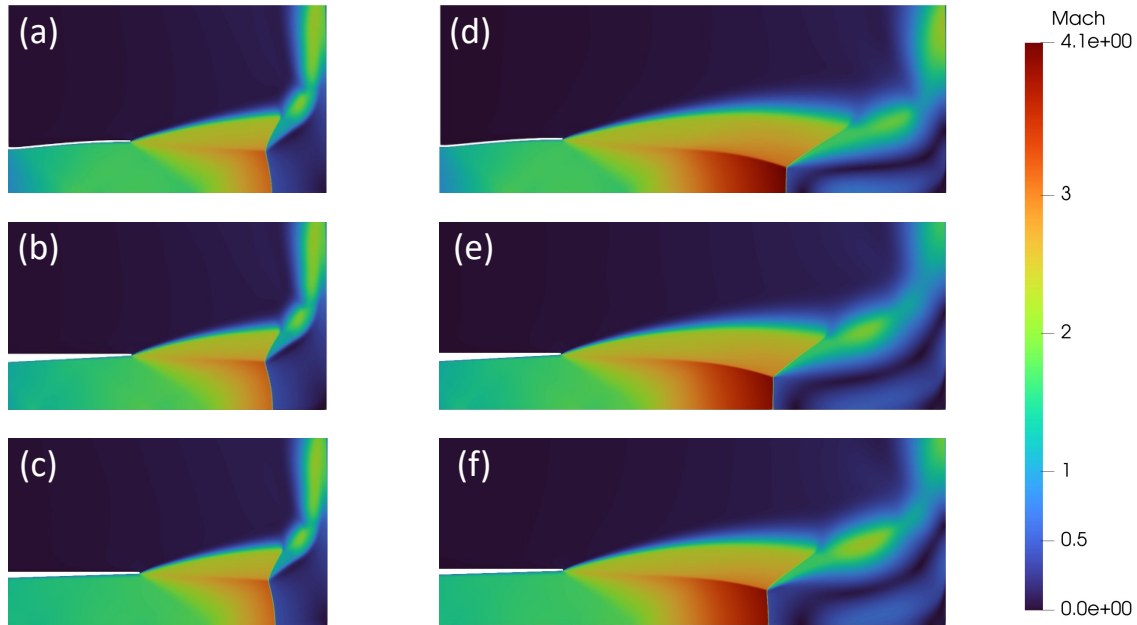


Figure 5.16: Mach number colour plots of an highly underexpanded impinging jet in cases of (a) N1, (b) N2, (c) N3 and D1 on the left; (d) N1, (e) N2, (f) N3 and D3 on the right.

Some differences in the flow behavior can be recognized as the wall distance is varying (see Figure 5.16). In fact, for distances D1 and D2 the formation of a fully developed shock cell is prevented by the proximity of the wall. As a result, the Mach disk that is normally generated in the free-jet results in this case anticipated, as well as enlarged in diameter. Moreover, the shape of the entire lambda-shock structure appears to be distorted, where in particular the inclination of the reflected shock (downstream the triple point) results more normal to the stream-wise direction compare to the free-jet case. The combination of these two characteristics leads to the formation of a wide subsonic area with no generation of a stagnation bubble, as shown in Figure 5.17,(a).

Contrarily, in case D3 the wall is far enough from the nozzle outlet to allow the formation of a fully developed shock cell. In this case, downstream the Mach disk the flow is not able to accelerate again to supersonic velocity due to the presence of the wall. As a consequence, it is in this case predicted the formation of a recirculation region, shown in Figure 5.17,(b). Additionally, the jump in Mach number is, coherently with the free-jet results, the highest for the nozzle N1.

Finally, for all the cases considered, the flow is redirected radially to form the wall-jet region. As previously done, the axial evolution of the Mach number and the pressure

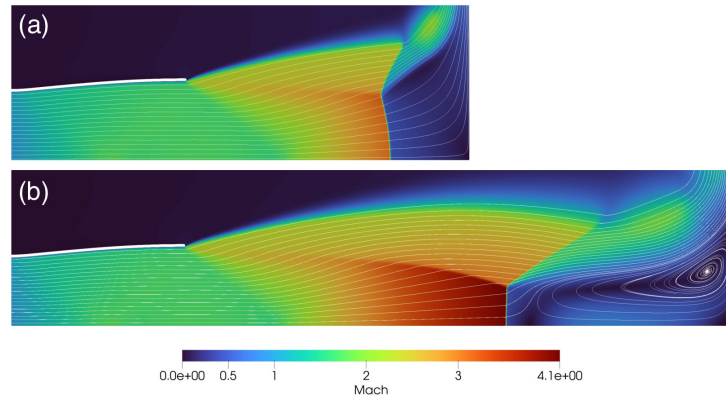


Figure 5.17: Visualization of the streamlines in case NPR2,N1 and distances D1(a), D3(b).

distribution generated over the plate are next inspected.

As shown in the graphs in Figure 5.18, the axial Mach number curves appear to be not relevantly sensible to the nozzle geometry for cases D1 and D2, while some discrepancies can be recognised for D3. Additionally, the absence of a stagnation point downstream the Mach disk at the short distances (D1 and D2) is a further confirm of the absence of the recirculation region. Contrarily, the Mach number behavior downstream the normal shock for distance D3 indicates the presence of a flow reversal area. Moreover, the axial location of the disk is, accordingly to the free-jet case, the largest for the contoured nozzle N1.

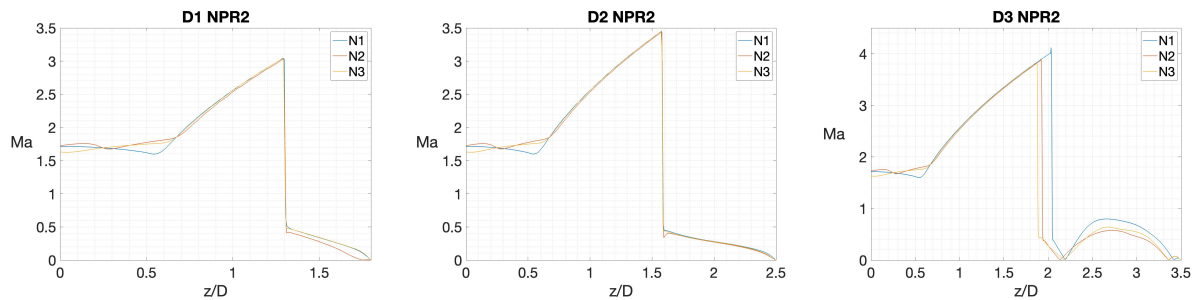


Figure 5.18: Axial Mach number evolution in cases of highly underexpanded jet impinging on a flat plate per different nozzle geometries.

The positioning of the wall has furthermore a relevant influence on the location of the Mach disk with respect the free jet case. With this regard, Figure 5.19 reports a comparison between the two configurations for the nozzle N2 and distances D2 and D3 (the same observations can be made for the other nozzles and distance D1).

The flow behavior appears coincident concerning the region upstream the discontinuity, while the Mach disk axial location is anticipated by the effect of the wall. In particular, for D3 the position of the shock is predicted within a difference of 14% compared to the

free-jet configuration, indicating that its axial location may be influenced by the presence of the wall.

The wall pressure distribution are reported in Figure 5.20, where the pressure is ex-

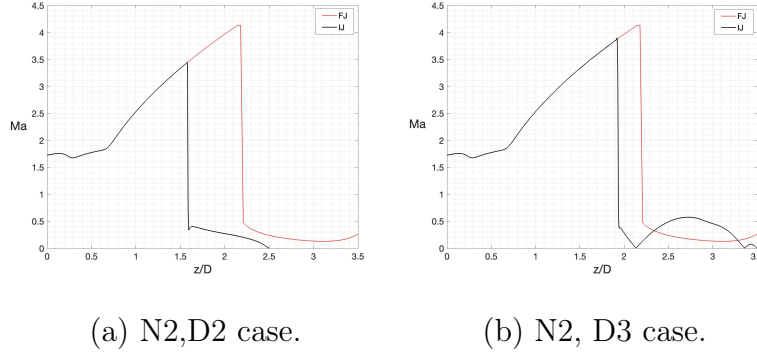


Figure 5.19: Comparison between the NPR2 axial Mach number evolution in cases of free jet (FJ) and impinging jet (IJ) configurations for nozzle N2 and distances D2 and D3.

pressed as the ratio between the local static pressure and the reservoir total pressure, than in case NPR2 is $P_0 = 1250308.5 Pa$.

As shown, the peak in pressure gradually shift from the centre-line (D1, no recirculation bubble) to an off-axis location (D3, recirculation bubble formed), while the pattern at nozzle-to-plate spacing D2 an almost flat behavior is predicted over the plate. The discrepancies in behavior due to the nozzle geometry are once again rather small whether the formation of the fully developed shock cell is prevented (D1 and D2), whereas notable differences exists when the wall is placed downstream the same shock (D3). In particular, the decrease in pressure is more marked for the conical nozzles, while lower losses are expected for the contoured one.

Finally, as seen for the moderately underexpanded jet, the curves behave similarly in the wall-jet region, irrespective the nozzle geometry.

For what concerns the axial evolution, one may say that the nozzle geometry has not a relevant influence especially at short distances (D2 and D3) where the results appear almost coincident, while some differences in the Mach disk location are numerically predicted for D3.

Radial wall-jet investigation:

At last, it is investigated the nozzle geometry effect on the wall-jet behavior. This is accomplished considering the velocities profiles along the wall at radial locations of $r/D = [1, 2, 3]$ for the moderately underexpanded jet (NPR1). The results reported in Figure 5.21 represents the profiles for all the considered radial location for the wall distance D1, while only the case $r/D = 1$ is illustrated regarding the case D3, since similar outcomes have

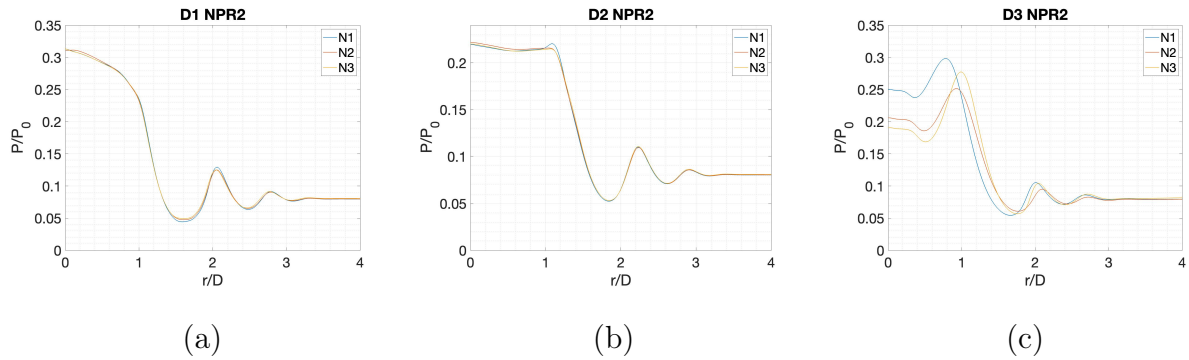


Figure 5.20: P/P_0 distributions over the flat plate in case of highly underexpanded jet per different nozzle geometries and distances. In the graphs, P_0 refers to the reservoir condition in case NPR2.

been obtained in the other cases and are hence here omitted. In particular the graphs show that, as expected, the radial jet is marginally influenced by the nozzle geometry closer to the impingement region $r/D = 1$, while the curves completely overlap as the flow moves further outward.

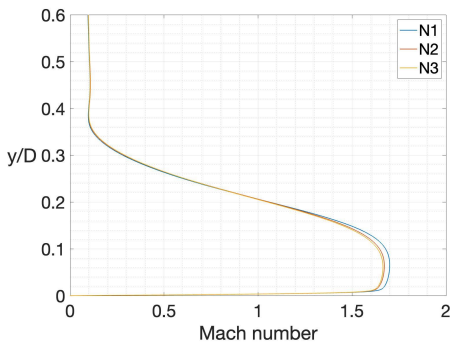
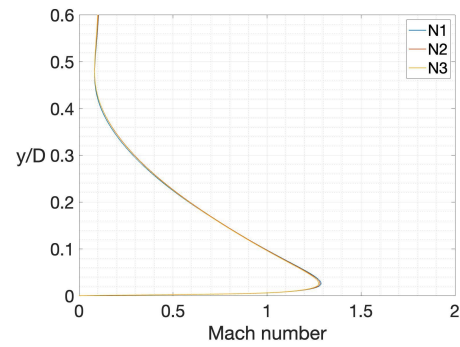
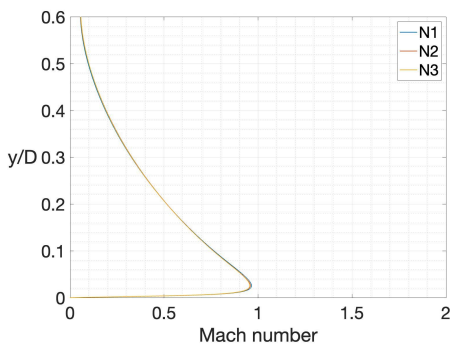
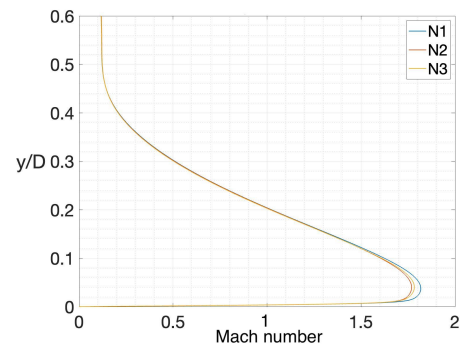
(a) D1, $r/D = 1$.(b) D1, $r/D = 2$.(c) D1, $r/D = 3$.(d) D3, $r/D = 1$.

Figure 5.21: Mach number profile corresponding to the radial wall-jet for different nozzle geometries. In the graphs, $y/D = 0$ corresponds to the position of the wall. The coordinate y/D grows moving axially away from the wall ($y = -z$).

6 | Conclusion and improvements

A numerical study on the shock structures for free and impinging underexpanded jet was carried out making use of the axisymmetric RANS solver of the CFD code SU2. Verification and validation are initially performed by proving results independence from the employed grid and verifying the accuracy in replicating real experimental data. The analysis of the results showed that the numerical set-up employed in this work is able to properly predict the behavior of the core region of the jet, as well as to predict the occurrence of stagnation bubble.

The performances in simulating moderately and highly underexpanded jets, in both free and impinging jets configurations, are evaluated for two popular turbulence models: the Spalart-Allmaras (SA) and the Shear Stress Transport (SST) by Menter. From the investigation of the simulations results, the SST appeared to not be consistent with the expected results for highly underexpanded jets, as it converged to a wrong solution. As a consequence, the SA turbulence model was employed for all the simulations of the final study contained in this work.

The impact of the nozzle geometry on the flowfield is then investigated for different operative conditions in terms of nozzle pressure ratio and nozzle-to-wall distance.

Referring to the obtained results, this work provides a numerical confirmation that the difference in flow throughout a convergent-divergent nozzle are not caused by the geometry itself of the divergence section but rather by the length and thickness of the boundary layer that develops on the internal wall of the device, as suggested by the flow uniformity across the outlet sections of the nozzles.

Moreover, it is found that the geometry might affect significantly the intensity of the shocks formed in the free-jet structure during the outflow expansion. In particular, it is found that the divergence angle of the divergent section of the nozzle might have an important role in defining the overall flow pattern, leading to the formation of small in size Mach disk even at low nozzle pressure ratio. Future improvements of this work might further investigate the effects of the divergence angle in the possible occurrence of Mach disks in the flow.

For what concerns the impinging-jet configuration, one might conclude that the discrep-

ancies in behavior are rather small when the formation of a fully developed shock cell is prevented, regardless to the nozzle pressure ratio and distance. On the other hand, when the shock cell is totally formed, the above-mentioned different intensities in the intercepting shock and Mach disk reflect on the behavior of the impingement region, as testified by the strength and distance from the wall of the plate shock, when formed.

Additionally, it is found that the nozzle geometry does not have a relevant influence on the development of the free-shear layer in the free-jet and in the radial wall-jet evolution in the impinging-jet.

All things considered, the performed simulations can be considered reliable to some extent in order to obtain some general conclusions. In the specific, one can say that the considered numerical method provides reliable results concerning moderately and highly underexpanded jets expanding in a free environment, although some uncertainties have been acknowledged to be present along the axis of symmetry. This errors could be caused by low resolution in the employed computational grid, which might be not sufficient to catch the very high gradients are expected to form along the centerline. A local refinement might represent a solution for the odd behavior along the axis. On the other hand, the results obtained in case of impinging jet showed overall reliable results in case of impinging jet, although the simulations hereby reported are not fully converged whether a Mach disk is formed in front of the wall (distance D3) and hence their results must be considered less accurate. A possible explanation for the stiff convergence of this case could be the intrinsically unstable behavior of this kind of flows, which makes the steady state simplification not suitable for representing their complete behavior.

Bibliography

- [1] R. Bunker, J. Dees, and P. Palafox. Impingement cooling in gas turbines: Design, applications, and limitations. *WIT Transactions on State-of-the-art in Science and Engineering*, 76:1–32, 2014.
- [2] H.H. Cho, K.M. Kim, and J. Song. Applications of impingement jet cooling systems. In *Cooling Systems, Energy, Engineering and Applications*, chapter 2, pages 37–67. Nova Science, 2011.
- [3] I. Nastase and F. Bode. Impinging jets – a short review on strategies for heat transfer enhancement. *E3S Web of Conferences*, 32:01013, 2018.
- [4] M. Grujicic, C.L. Zhao, C. Tong, W.S. DeRosset, and D. Helfritch. Analysis of the impact velocity of powder particles in the cold-gas dynamic-spray process. *Materials Science and Engineering: A*, 368:222–230, 2004.
- [5] L. Myers, N. Rudenko, and D. Mclaughlin. Investigation on the flow-field of two parallel round jets impinging normal to a flat surface. 54th AIAA Aerospace Sciences Meeting, San Diego, CA, AIAA 2016-1776, 2016.
- [6] M. Harmon, V. N. Bhargav, P. Sellappan, F. Alvi, and R. Kumar. Experimental study of impinging jet flow field involving converging and cd nozzle pair. 2018 AIAA Aerospace Sciences Meeting, Kissimmee, FL, AIAA 2018-0261, 2018.
- [7] N. Karthikeyan and L. Venkatakrisnan. Flow field and acoustic investigations of the launch vehicle environment during lift-off. 21st AIAA/CEAS Aeroacoustics Conference, Dallas, TX, AIAA 2015-3121, 2015.
- [8] N. Karthikeyan and L. Venkatakrisnan. Acoustic characterization of jet interaction with launch structures during lift-off. *Journal of Spacecraft and Rockets*, 54:1–12, 2017.
- [9] A. Kagenov, A. Glazunov, K. Kostyushin, I. Eremin, and V. Shuvarikov. Numerical investigation of the effect of the configuration of ExoMars landing platform propulsion system on the interaction of supersonic jets with the surface of Mars. American

- Institute of Physics Conference Series. XXV Conference on High-Energy Processes in Condensed Matter, Novosibirsk, RU, 2017.
- [10] C. DUP. Donaldson and R. S. Snedeker. A study of free jet impingement. part 1. mean properties of free and impinging jets. *Journal of Fluid Mechanics*, 45:281–319, 1971.
- [11] J. Gummer and L. Hunt. The impingement of a uniform, axisymmetric, supersonic jet on a perpendicular flat plate. *The Aeronautical Quarterly*, 22:403–420, 1971.
- [12] J. C. Carling and B. L. Hunt. The near wall jet of a normally impinging, uniform, axisymmetric, supersonic jet. *Journal of Fluid Mechanics*, 66:159–176, 1974.
- [13] J. Iwamoto. Impingement of Under-Expanded Jets on a Flat Plate. *Journal of Fluids Engineering*, 112:179–184, 1990.
- [14] P. J. Lamont and B. L. Hunt. The impingement of underexpanded, axisymmetric jets on perpendicular and inclined flat plates. *Journal of Fluid Mechanics*, 100:471–511, 1980.
- [15] Y. Goto, K. McIlroy, T. Nonomura, and K. Fujii. Detailed analysis of flat plate pressure peaks created by supersonic jet impingements. 47th AIAA Aerospace Sciences Meeting including The New Horizons Forum and Aerospace Exposition, Orlando, FL, AIAA 2009-1289, 2009.
- [16] Y. Nakai, N. Fujimatsu, and K. Fujii. Experimental study of underexpanded supersonic jet impingement on an inclined flat plate. *AIAA Journal*, 44:2691–2699, 2006.
- [17] A. Krothapalli, E. Rajkuperan, F. Alvi, and L. Lourenco. Flow field and noise characteristics of a supersonic impinging jet. *Journal of Fluid Mechanics*, 392:155–181, 1999.
- [18] F. Alvi, J.A. Ladd, and W. Bower. Experimental and computational investigation of supersonic impinging jets. *AIAA Journal*, 40:599–609, 2002.
- [19] S.I. Kim and S. Park. Unsteady flow simulation of supersonic impinging jet. 41st Aerospace Sciences Meeting and Exhibit, Reno, NV, AIAA 2003-621, 2003.
- [20] R.C. Chin, M. Li, C. Harkin, T. Rochwerger, L. Chan, A. Ooi, A. Risborg, and J. Soria. Investigation of the flow structures in supersonic free and impinging jet flows. *Journal of Fluids Engineering*, 135:031202, 2013.
- [21] B. Henderson, J. Bridges, and M. Wernet. An experimental study of the oscilla-

- tory flow structure of tone-producing supersonic impinging jets. *Journal of Fluid Mechanics*, 542:115–137, 2005.
- [22] K. Hatanaka and T. Saito. Influence of nozzle geometry on underexpanded axisymmetric freejet characteristics. *Shock Waves*, 22:427–434, 2012.
- [23] Y. Otobe, H. Kashimura, S. Matsuo, T. Setoguchi, and Kim H.-D. Influence of nozzle geometry on the near-field structure of a highly underexpanded sonic jet. *Journal of Fluids and Structures*, 24:281–293, 2008.
- [24] M. Kaushik. Wave phenomena. In *Fundamentals of Gas Dynamics*, chapter 5, pages 193–295. Springer Singapore, Singapore, 2022.
- [25] A.H. Shapiro. *The Dynamics and Thermodynamics of Compressible Fluid Flow*, volume 1. The Ronald Press Co, New York, 1953.
- [26] E. Franquet, V. Perrier, S. Gibout, and P. Bruel. Free underexpanded jets in a quiescent medium: A review. *Progress in Aerospace Sciences*, 77:25–53, 2015.
- [27] E. M. Greitzer, C. S. Tan, and M. B. Graf. Boundary layers and free shear layers. In *Internal Flow: Concepts and Applications*, Cambridge Engine Technology Series, page 166–216. Cambridge University Press, Cambridge, 2004.
- [28] P. S. Cumber, M. Fairweather, S. A. E. G. Falle, and J. R. Giddings. Predictions of the structure of turbulent, moderately underexpanded jets. *Journal of Fluids Engineering*, 116:707–713, 1994.
- [29] P. S. Cumber, M. Fairweather, S. A. E. G. Falle, and J. R. Giddings. Predictions of the structure of turbulent, highly underexpanded jets. *Journal of Fluids Engineering*, 117:599–604, 1995.
- [30] M. Abbett. Mach disk in underexpanded exhaust plumes. *AIAA Journal*, 9:512–514, 1971.
- [31] C.-W. Jiang, T. Han, Z. Gao, and C.-H. Lee. A review of impinging jets during rocket launching. *Progress in Aerospace Sciences*, 109:100547, 2019.
- [32] P. S. Cumber, M. Fairweather, S. A. E. G. Falle, and J. R. Giddings. Predictions of impacting sonic and supersonic jets. *Journal of Fluids Engineering*, 119:83–89, 1997.
- [33] B. Henderson. The connection between sound production and jet structure of the supersonic impinging jet. *The Journal of the Acoustical Society of America*, 111:735–747, 2002.

- [34] F. Palacios, M. Colonna, A. Aranake, A. Campos, S. Copeland, T. Economon, A. Lonkar, T. Lukaczyk, T. Taylor, and J. Alonso. Stanford university unstructured (su2): An open-source integrated computational environment for multi-physics simulation and design. 51st AIAA Aerospace Sciences Meeting including the New Horizons Forum and Aerospace Exposition, Dallas, TX, AIAA 2013-0287, 2013.
- [35] T. Economon, F. Palacios, S. Copeland, T. Lukaczyk, and J. Alonso. Su2: An open-source suite for multiphysics simulation and design. *AIAA Journal*, 54:828–846, 2016.
- [36] Comsol Documentation. Sutherland’s law. https://doc.comsol.com/5.5/doc/com.comsol.help.cfd/cfd_ug_fluidflow_high_mach.08.27.html, 2022. [Online; accessed 07-2022].
- [37] A. Balabel, A.M. Hegab, M. Nasr, and Samy M. El-Behery. Assessment of turbulence modeling for gas flow in two-dimensional convergent–divergent rocket nozzle. *Applied Mathematical Modelling*, 35:3408–3422, 2011.
- [38] Langley Research Center. Turbulence modeling resource. <https://turbmodels.larc.nasa.gov/index.html>, 2022. [Online; accessed 08-2022].
- [39] CFD Online. Boussinesq eddy viscosity assumption. https://www.cfd-online.com/Wiki/Boussinesq_eddy_viscosity_assumption. [Online; accessed 08-2022].
- [40] P. Spalart and S. Allmaras. A one-equation turbulence model for aerodynamic flows. *AIAA*, 439, 1992.
- [41] F. R. Menter. Two-equation eddy-viscosity turbulence models for engineering applications. *AIAA Journal*, 32:1598–1605, 1994.
- [42] Langley Research Center Turbulence Modeling Resource. The spalart-allmaras turbulence model. <https://turbmodels.larc.nasa.gov/spalart.html#sa>, 2022. [Online; accessed 08-2022].
- [43] Langley Research Center Turbulence Modeling Resource. Implementing turbulence models into the compressible rans equations. <https://turbmodels.larc.nasa.gov/implementrans.html>, 2021. [Online; accessed 08-2022].
- [44] S.R. Allmaras, F.T. Johnson, and P.R. Spalart. Modifications and clarifications for the implementation of the spalart-allmaras turbulence model. 7th International Conference on Computational Fluid Dynamics, Big Island, HI, ICCFD7-1902, 2012.
- [45] P. Catalano and M. Amato. An evaluation of rans turbulence modelling for aerodynamic applications. *Aerospace Science and Technology*, 7:493–509, 2003.

- [46] Langley Research Center Turbulence Modeling Resource. The menter shear stress transport turbulence model. <https://turbmodels.larc.nasa.gov/sst.html>, 2021. [Online; accessed 08-2022].
- [47] P.R. Spalart and C.L. Rumsey. Effective inflow conditions for turbulence models in aerodynamic calculations. *AIAA Journal*, 45:2544–2553, 2007.
- [48] T. Barth and D. Jespersen. The design and application of upwind schemes on unstructured meshes. 27th Aerospace Sciences Meeting, Reno, NV, 1989.
- [49] Convergence to steady state solutions of the euler equations on unstructured grids with limiters. *Journal of Computational Physics*, 118:120–130, 1995.
- [50] K. Kitamura. Reconstruction and slope limiters. In *Advancement of Shock Capturing Computational Fluid Dynamics Methods: Numerical Flux Functions in Finite Volume Method*, pages 117–136. Springer Singapore, Singapore, 2020.
- [51] Gmsh 4.10.5 reference manual. <https://gmsh.info/doc/texinfo/gmsh.html#Obtaining-Gmsh>, 2022. [Online; accessed 08-2022].
- [52] Wikipedia contributors. Law of the wall — Wikipedia, the free encyclopedia. https://en.wikipedia.org/w/index.php?title=Law_of_the_wall&oldid=1087128201, 2022. [Online; accessed 07-2022].
- [53] T. R. Troutt and D. K. Mclaughlin. Experiments on the flow and acoustic properties of a moderate-reynolds-number supersonic jet. *Journal of Fluid Mechanics*, 116:123–156, 1993.
- [54] Overview of cfd verification and validation. <https://www.grc.nasa.gov/www/wind/valid/tutorial/overview.html>, 2021. [Online; accessed 08-2022].

List of Figures

2.1	Schematic illustration of the flow field zones of an underexpanded jet. . . .	9
2.2	Structure of a moderately underexpanded jet.	10
2.3	Structure of a highly underexpanded jet.	12
2.4	Structure of a very highly underexpanded jet.	13
2.5	Overexpanded jet during a SpaceX Raptor Engine Test.	13
2.6	Moderately underexpanded (a) and highly underexpanded (b) impinging jet schemes.	16
2.7	Positions of shock structures at varying impingement distances [31], where h_{s1} and h_{s2} are the distances of the reflected shock intersection with the constant pressure line and h_s is the one of the plate shock from the nozzle exit plane.	17
3.1	Magnification of the nozzle region of the computational grid used in case of supersonic jet released in a free environment, where a refinement box can be seen downstream of the nozzle and the wall-mesh on its internal wall.	27
4.1	Computational domain and boundary conditions used to validate the free flow case.	31
4.2	Axial Mach number per different mesh refinements - Free flow case.	32
4.3	$mesh_4$ used for validating the free flow.	33
4.4	Mach Number and Static Pressure distribution along the outlet corresponding to the nozzle used in [53]	33
4.5	Colour plot of the Mach number field obtained replicating numerically the experimental set-up of Troutt and McLaughlin [53] with magnification of the nozzle outlet region.	34
4.6	Axial Mach number per different turbulence models compared with the results of [20].	35

4.7	Comparison of the streamwise Mach number profiles in the radial direction at different axial location obtained with different turbulence models. The results are compared with the experimental data reported in Troutt and McLaughlin [53]. (a) $z/D = 1$, (b) $z/D = 5$, (c) $z/D = 10$, and (d) $z/D = 15$	36
4.8	Axial location of the plots reported in Figure 4.7.	36
4.9	Colour plot of the eddy viscosity in case of SA (a) and SST (b) turbulence model.	38
4.10	Computational domain and boundary conditions used to validate the impinging flow case.	39
4.11	Axial Mach number per different mesh refinements - Impinging flow case.	40
4.12	Computational grid used to validate the impinging flow case.	41
4.13	Location of the sonic line (a) and the iso-pressure line at $P = 3.57P_\infty$ (b) across the outlet section of the convergent nozzle.	42
4.14	Colour plot of the Mach number in case of highly underexpanded jet and impingement distance $z/D = 7.3$	43
4.15	Streamlines in case of highly underexpanded jet and impingement distance $z/D = 7.3$	43
4.16	Comparison of stagnation region pressure distribution over the plate with the experimental results of Donaldson and Snedeker [10], where the reference pressure P_0 is the centre-line stagnation pressure over the plate.	44
4.17	Comparison of the pressure coefficient distribution over the flat plate located at $z/D = 23.5$ with the experimental results of Donaldson and Snedeker [10] and the numerical results of [20].	45
4.18	Axial Mach number evolution across the Mach disk in cases of SA and SST turbulence model.	46
4.19	Colour plots of the turbulent viscosity in case of SA (a) and SST (b) turbulence models in case of $z/D = 7.3$	47
5.1	Illustration of half a section of the nozzles with their total length, where: (a) N1; (b) N2;(c) N3.	50
5.2	Computational grid and boundary conditions employed in case of contoured nozzle and distance D3.	52
5.3	Comparison between the exit mach number profile corresponding to three different nozzle shapes.	53
5.4	Color plot of the Mach number of a moderately underexpanded jet NPR1 in cases of (a) N1; (b) N2; (c) N3.	54

5.5	Axial Mach number evolution in case of NPR1 for different nozzle geometry.	55
5.6	Comparison of the streamwise Mach number profiles in the radial direction for different nozzle geometries at different axial locations in case of NPR1. In the graph R_e refers to the radius of the outlet section. On the bottom, a visualization of the location of the radial lines.	56
5.7	Color plot of the Mach number of a highly underexpanded jet NPR2 in cases of (a) N1; (b) N2; (c) N3.	57
5.8	Axial Mach number evolution in case of NPR2 for different nozzle geometry.	58
5.9	Comparison of the streamwise Mach number profiles in the radial direction per different nozzle geometry at different axial locations in case of NPR2. In the graph R_e refers to the radius of the outlet section. On the bottom, a visualization of the location of the radial lines.	59
5.10	Mach number colour plots of an impinging moderately underexpanded jet in cases of (a) N1, (b) N2, (c) N3 and D1 on the left; (d) N1, (e) N2, (f) N3 and D3 on the right.	60
5.11	Mach number axial evolution in case NPR1 impinging jet on a flat plate per different nozzle geometries.	61
5.12	Comparison between the NPR1 axial Mach number evolution in cases of free jet (FJ) and impinging jet (IJ) configurations for different nozzle geometries.	63
5.13	Visualization of the total pressure loss across the domain in case of N1, D1 and NPR1.	64
5.14	Visualization of the streamlines in case NPR1,N1 and D1.	64
5.15	P/P_0 distributions over the flat plate in case of moderately underexpanded jet NPR1 per different nozzle geometries and distances. In the graphs, P_0 refers to the reservoir condition.	65
5.16	Mach number colour plots of an highly underexpanded impinging jet in cases of (a) N1, (b) N2, (c) N3 and D1 on the left; (d) N1, (e) N2, (f) N3 and D3 on the right.	66
5.17	Visualization of the streamlines in case NPR2,N1 and distances D1(a), D3(b).	67
5.18	Axial Mach number evolution in cases of highly underexpanded jet impinging on a flat plate per different nozzle geometries.	67
5.19	Comparison between the NPR2 axial Mach number evolution in cases of free jet (FJ) and impinging jet (IJ) configurations for nozzle N2 and distances D2 and D3.	68

- 5.20 P/P_0 distributions over the flat plate in case of highly underexpanded jet per different nozzle geometries and distances. In the graphs, P_0 refers to the reservoir condition in case NPR2. 69
- 5.21 Mach number profile corresponding to the radial wall-jet for different nozzle geometries. In the graphs, $y/D = 0$ corresponds to the position of the wall. The coordinate y/D grows moving axially away from the wall ($y = -z$). . . 70

List of Tables

4.1	Computational parameters in case of free jet.	31
4.2	Values of h and respective number of cells.	32
4.3	Computational parameters in case of free jet.	39
5.1	Computational parameters used in all the computations.	51
5.2	Stand-off shock distance for different nozzle shapes and different wall distances. The value of δ is non-dimensional with respect the nozzle outer diameter D	62

Acknowledgements

Vorrei ringraziare il Professor K. Hillewaert per i consigli e il sostegno che mi ha sempre fornito con gentilezza durante tutta la durata della collaborazione. Ringrazio anche il Professor L. Vigevano, che ha accettato di essere il mio relatore e mi ha dato l'opportunità di completare questo lavoro.

Grazie agli amici del Politecnico per aver condiviso con me il cammino e per l'infinito numero di esperienze passate insieme. Avete reso tutto questo molto speciale.

Un ringraziamento speciale ad Andrea, vero compagno e spalla, sempre al mio fianco. Grazie anche ad Alex, per aver reso speciali le mie giornate.

Infine, un grazie di cuore anche i miei genitori e mia sorella, per avermi dato la possibilità di arrivare fin qui e per avermi sostenuto nel bene e nel male dandomi la forza di completare questo lavoro.

